1

IR Spectra in Space Observation

The IR (infrared) range corresponds to the frequency band between 10^4 GHz and 5×10^5 GHz, therefore to wavelengths ranging between 0.78 µm and 1,000 µm. According to the ISO system (ISO 20473, 2007), this range is divided into three regions corresponding to near IR from 780 nm to 3,000 nm (sunlight), mid-IR from 3 µm to 50 µm (thermal source) and far IR from 50 µm to 1,000 µm (source in astronomy). For a given electronic state, the interaction between an electromagnetic wave in this range and a physical system in gas, liquid, solid or possibly plasma state is reflected by a transition between two vibrational and/or rotational energy states of the system, which are discrete and/or in the continuum. The possible physico-chemical processes, such as the absorption and emission of photons, elastic (Rayleigh) scattering and inelastic (Raman, Compton) scattering, dissociation, ionization and various possible combinations and interferences of these phenomena can be observed using optical instruments, such as spectrometers or telescopes. These instruments can operate on site in a laboratory or from an observatory or in the space (aboard a space probe). Depending on the latter sites and the system under observation, various options should be considered for the successful completion of an observation process.

1.1. Introduction

In a laboratory, experimental IR spectroscopy of atmospheric molecules is mainly studied in the gas phase.

Taking into account the shape of the absorption line (Gaussian by Doppler effect, Lorentzian by pressure-induced broadening) [DAH 88, DAH 97, DAH 16a, DAH 17], the intensity of a vibration–rotation absorption line in the gas phase is given by the expression:

$$S_{if}^{g} = \int_{\sigma_{\min}}^{\sigma_{\max}} \frac{8\pi^3}{3hc} \sigma_{if} f(\sigma - \sigma_{if}) N \left[1 - \exp\left(-\frac{hc}{k_B T}\sigma_{if}\right)\right] g_i \frac{\exp(-hc\sigma_i / k_B T)}{Q(T)} R_{if}^2 \, d\sigma \qquad [1.1]$$

where σ_{if} is the wave number (in cm^{-1}) of the considered rovibrational transition, N is the number of molecules per unit volume, $hc\sigma_i$ is the energy of the initial level, $Q(T)$ is the total partition function of the molecule at temperature T, R_{if} is the moment of rovibrational transition, and finally g_i is the degeneracy due to the nuclear spin of the initial level. The shape of the line is a Voigt function, a convolution product of a Gaussian and a Lorentzian, as the Doppler effect and the broadening by pressure are concomitant, and its integral over the absorption domain is equal to 1 ($1 = \int_{\sigma_{\min}}^{\sigma_{\max}} f(\sigma - \sigma_{if}) \, d\sigma$).

In condensed media, when the observed molecule is trapped in a rare gas matrix or in a nanocage of a solid medium, a corrective term reflecting the effect of the refractive index n of the solid medium must be taken into account. If the rotation–vibration interaction is ignored, and the fundamental state is not degenerate ($g_0 = 1$), the intensity of a vibrational line at low temperature, in relation with a molecule is written as:

$$S_{if}^{m} = \int_{\sigma_{\min}}^{\sigma_{\max}} \frac{1}{n} \left(\frac{n^2+1}{3}\right)^2 \frac{8\pi^3}{3hc} \sigma_{if} f(\sigma - \sigma_{if}) \left|R_{if}\right|^2 \, d\sigma \qquad [1.2]$$

where R_{if} is the vibrational transition moment. Written in this form, relation 1.2 provides essential information about the dipole transition moments of the vibrational modes in a solid matrix. These quantities can be extracted experimentally from the integrated intensity of the absorption spectrum:

$$S_{if}^{m} = \frac{1}{2lN} \int Ln \frac{I_0(\sigma - \sigma_{if})}{I_t(\sigma - \sigma_{if})} d\sigma = \frac{1}{2lN} I_{if} \qquad [1.3]$$

where N is the number of molecules per cm^3, $2l$ is the path length in the sample, and the term under the integral is the integrated absorption measured over the IR absorption spectrum domain. The calculation of physical quantities, such as the lifetime of a level based on the integrated absorption, is explained in chapters 6 and 7 of [DAH 16a] and in the Phd dissertations [ABO 73a, DUB 75, GAU 80, BOI 85] for molecules inserted in a solid rare gas matrix. For dipole moments, the method is given, for example, in [DAH 88] for CO_2 and N_2O molecules in the gas phase, or [GHE 79] for the CH_4 molecule.

Chapter 3 of Volume 1 of this series provides a description of the method for the measurement and analysis of an absorption line based on the Bouguer–Lambert law, applied to determine the infinitesimal amount of energy absorbed by an elementary thickness of matter. For an intensity $I(\sigma)$ of a radiation of wave number σ traveling through an elementary thickness dl of a gas under pressure P, the resulting variation $dI(\sigma)$ is proportional to $I(\sigma)$ and dl. These hypotheses lead to the following Bouguer–Lambert law:

$$dI(\sigma) = -k(\sigma,P)\,I(\sigma)\,dl \qquad [1.4]$$

where $k(\sigma, P)$ is the absorption coefficient at wave number σ and pressure P. The intensity of the radiation transmitted at wave number σ results from the integration of the previous equation:

$$I_t(\sigma) = I_0(\sigma)\,e^{-k(\sigma,P)l} \qquad [1.5]$$

where $I_0(\sigma)$ is the intensity of the radiation incident on the gas and l is the gas thickness through which the radiation travels.

The actual shape of an absorption line is defined by the following function:

$$A(\sigma) = \frac{I_a(\sigma)}{I_0(\sigma)} = 1 - \frac{I_t(\sigma)}{I_0(\sigma)} \qquad [1.6]$$

which does not take into account the instrumental line shape (infinite resolution hypothesis), with $I_a(\sigma) = I_0(\sigma)\text{-}I_t(\sigma)$, where $I_a(\sigma)$ is the intensity of the absorbed radiation.

The previous two equations lead to:

$$A(\sigma) = 1 - e^{-k(\sigma,P)l} \qquad [1.7]$$

Moreover, the profile of the spectral line is defined by the variation of the absorption coefficient $k(\sigma, P)$, which depends on the wave number σ and is given by:

$$k(\sigma,P) = \frac{1}{l}\ln\left(\frac{I_0(\sigma)}{I_t(\sigma)}\right) \qquad [1.8]$$

For a number of active molecules absorbing or emitting weak radiation, leading to the property $k(\sigma, P)\, l \ll 1$, the actual shape of the line coincides with the profile and is expressed as:

$$A(\sigma) \approx k(\sigma, P)l \qquad [1.9]$$

This expression is valid in the real space of the spectrum. In the measurement space, the effect of the instrumental line shape leads to an apparent shape, which is the convolution product of the instrumental line shape and the actual shape. A deconvolution process is required to retrieve the actual spectrum.

The integrated absorption coefficient of the line is defined from its actual profile, by integration over the absorption domain, which is as follows:

$$S = \int_0^\infty k(\sigma, P)\, d\sigma \qquad [1.10]$$

If the active molecules absorb independently of one another (Beer's hypothesis), this coefficient is proportional to the pressure and is written as:

$$S = S^0 P \qquad [1.11]$$

where S^0 is known as the "line intensity".

It is important to note that Beer's hypothesis is not generally verified for each wave number, and as a result, the integrated absorption coefficient is not proportional to the pressure for each wave number. This experimentally determined coefficient is related to the theoretical coefficients expressed by equations [1.1] and [1.2].

The absorption lines corresponding to transitions between energy levels can be determined experimentally, either by frequency-resolved spectroscopy using a spectrometer or an interferometer, or by laser absorption over the absorption spectral range of the line. The recorded spectra are the convolution product of the instrumental line shape and the actual shape of the absorption line. A deconvolution of these spectra is required before the analysis, in terms of the intensity, width and center of the line. The procedure is described in Appendix 1 (section 1.6.1) and relies on the application of the sampling theorem.

Building a setup for experimental observation requires three elements.

The first element is a set containing a light source and a dispersive element for the frequency scanning of the spectral range, if the source is polychromatic. There are classical sources (spectral lamp, black body, etc.) or quantum sources (lasers). The classical light source can be a natural heat source, such as the light from a star or an artificial one, or light emitted by a gas lamp or a heated filament. These are wide spectral band polychromatic sources, whose maximum intensity corresponds to a given wavelength λ_m, which depends on the temperature T according to the law $\lambda_m T$ = constant. For a black body, the constant in Wien's displacement law is equal to 2.897 773 10^{-3} mK. The laser quantum sources are also used in IR spectroscopy in experiments studying system dynamics under radiation, such as laser-induced fluorescence, double resonance (DR), Rayleigh or Raman scattering or the dynamics of radiative or non-radiative relaxation of the populations of energy levels in probe–pump experiments. These are monochromatic or quasi-monochromatic sources of narrow spectral band. A tunable laser can be used to determine the absorption spectrum around a frequency defined by the transition between two energy levels. Resonant cavity spectroscopy, developed as a result of efforts to improve laser sources, involves the insertion of an absorbing molecule in the laser cavity, and then the identification of the absorption due to losses in the laser gain curve.

The second element is the system to be analyzed can be a fluid (gas or liquid), a solid or a plasma medium in a suitable laboratory chamber, or in a natural medium in space. Laboratory settings sometimes use absorption cells filled with fluid (gas or liquid) or a sample holder's surface on which the solid medium is deposited. A multiple-reflection cell is used to increase the absorption path when the transition is weak, in order to reach a convenient signal-to-noise ratio (SNR) for the observation of the absorption line.

Finally, the third element is a data detection and acquisition system that translates the transition induced at each frequency of the incident light on the studied systems into an electrical signal, which after analysis allows the characterization of the system based on its spectral signature.

In formal terms, the experimental setup includes an object space, which is the illuminated system, or an image space, which contains the devices for detection and those of the optical system, which is the set of optical devices in the measurement instrument. IR vibrational and rotational spectroscopy focuses on the processes of photon absorption or emission in a spectral range of low energy molecular spectroscopy. This domain is broader than that corresponding to the IR range, since it spans from microwaves to ultraviolet radiation.

The instruments used in IR spectroscopy essentially rely on electromagnetic wave interferences, in order to separate the spectral components of the radiation from a classical light source and determine the effect of the observed system on each spectral element used as a probe. These are generally prism spectrographs, grating spectrometers, Michelson interferometers or frequency- and time-resolved laser spectroscopy, since laser development [DEM 96].

This chapter focuses on observation and measuring techniques. The techniques that are essentially used in laboratories for measuring campaigns involve interferential spectroscopy, the use of gratings, laser spectroscopy or polarized light spectroscopy. The chapter ends with an example of the device used on the Mars Express and Venus Express orbiters.

Section 1.2 is dedicated to Fourier transform infrared spectroscopy (FTIR). Given the rich bibliographical references on the subject, only the first works in this field are referenced [JAC 60, BRA 95, CON 66, LOE 66, HUN 68, BEL 72a, CHA 73, GRI 75, GRI 86, DEM 96, JAM 02]. This section includes a description of the operating elements related to technical aspects in the setup for observation or data analysis. Two types of interferometers are described, a laboratory interferometer and a commercial interferometer.

First, a Connes-type Fourier transform interferometer (FTIR) with a very large path difference is described. This apparatus was built at the Molecular Spectronomy Laboratory at the Sorbonne University in Paris, Pierre and Marie Curie campus (formerly Pierre and Marie Curie University). This instrument was operational for the study of gas phase molecules in the atmosphere until the beginning of the 21st century, under the leadership of L. Henry, according to a concept proposed by P. Connes and developed by Valentin and Michel. A model of this type of interferometer is still operational in the Molecular and Atmospheric Spectrometry Group at Reims University. It is important to note that P. Connes, who worked at the Aimé-Cotton Laboratory at Paris Saclay University (formerly Paris South University, of Orsay) and the Director of LAC of that time, Jacquinot have made significant contributions to the development of Fourier transform spectroscopy [CON 92, CON 95].

A commercial type (Brucker IFS 113v) FTIR used in research work on the spectroscopy of molecular species isolated in an inert matrix is also described. The experimental device was used to study a certain number of atmospheric molecules using the isolated matrix technique, by the group led by L. Abouaf-Marguin and L. Schriver-Mazuoli at the Laboratory of Molecular Physics and Applications of Sorbonne University in Paris (formerly Pierre and Marie Curie University in Paris) at the beginning of the 1990s [BRO 93a, ABD 93, LUG 94, DES 94, JAS 95, RAD 95, DAH 97, BAH 97, HAL 98, CHA 00a, CHA 01, COA 03].

The spectroscopy of laser absorption in a resonant cavity is another example of spectroscopy that differs from the classical frequency-resolved and dispersion spectroscopy, using prisms or interference with echelette grating. Further examples are the resonant cavity laser absorption spectroscopy of the intracavity laser absorption spectroscopy (ICLAS) type, or the cavity ring-down spectroscopy (CRDS). These techniques can be used to measure weak absorptions. In France, these techniques were mainly developed by the Interdisciplinary Laboratory of Physics at Joseph Fourier University of Grenoble (LIPhy, former Spectrometry Laboratory) [STO 52, CHE 83, CAM 86, CAM 90, CAM 91, ROM 93, ROM 97a]. It is worthwhile to highlight the pioneering work of the LIPhy researchers in the development of cutting-edge laser techniques and instruments for molecular absorption spectroscopy, such as the continuous wave cavity in ring-down spectroscopy (CW-CRDS) [MOR 05], optical-feedback cavity-enhanced absorption spectroscopy (OFCEAS) [ROM 97a] and mode-locked cavity-enhanced absorption spectroscopy (ML-CEAS) [GHE 02], which were invented or developed for the first time at LIPhy, or the use of a quantum cascade diode [GOR 13] or frequency combs to improve the limits of detection [MON 15]. One section focuses on frequency comb spectroscopy (FCS), which is increasingly used to study molecules [HÄN 06, HAL 06, CUN 01, FOR 19, DID 20].

Section 1.4 provides examples of techniques that were applied for the study of molecules in the atmospheres of planets other than the Earth. It includes a brief description of the spectroscopic ellipsometry technique [AZZ 77], which is used for the study of materials deposited as thin layers on substrates. This technique was used to determine the optical indices of aerosols present in the atmospheres of planets or satellites such as Titan (“tholins”) [SCI 10, CAR 12, MAH 11, SCI 12, MAH 12a, MAH 12b, MAH 12c, MAH 14]. The final part of the section briefly describes the SOIR device used on the Venus Express for the study of the atmosphere of Venus. For the observations conducted from a space probe, an example is the observation device referred to as SPICAM (“Spectroscopy for Investigation of Characteristics of the Atmosphere of Mars”) or SPICAV/SOIR (Solar Occultation in the Infra-Red) aboard the orbiters (Mars Express/Venus Express) and developed (formerly Aeronomy Service SA and former Center for Earth and Planetary studies) in collaboration with Belgian and Russian partners, under the main coordination of Bertaux [NEV 06, BER 07, MAH 08, VIL 08a].

1.2. Fourier transform spectroscopy

Since the development of the first interferometer by Michelson at the end of the 19th century [MIC 81, MIC 82], interferometric spectroscopy or Fourier transform spectroscopy using interferometers has gradually replaced classical spectroscopy, by grating spectrometers for the measurement and analysis of absorption spectra in the

IR range. The technique of interferometric spectroscopy, later referred to as Fourier transform spectroscopy, was proposed by Jacquinot [JAC 60, CON 92] in the 1960s. The state-of-the-art for the optical field in France in the 1960s can be found in [AMA 62]. Jacquinot [JAC 60] describes the methods for selecting wavelengths by the frequency of interferometric modulation. The spectrum is not directly recorded in its common form, but in the form of an interferogram that is the Fourier transform of the spectrum. Similar to the photographic methods, the main advantage of this method is that the time required for recording the interferogram does not depend on the width of the spectral range. The resolution and the luminosity of the measuring process are considered, as well as the various methods for spectrum reconstruction from the interferogram.

The evolution of grating spectrometers or spectrographs towards interferometers was made possible by the works of the following scientists:

– Fellgett [FEL 49, FEL 58] on the advantages of the “multiplex” method or Fellgett’s advantage; at each time t, an FTIR spectrometer simultaneously records the spectral data at all of the wavelengths at high resolution, over an extended spectral range. A grating spectrometer or a spectrograph measures the intensity of an absorption or emission line over a very narrow spectral range around a given wavelength, during the measurement of a signal whose noise is mainly that of the detector. A multiplex measurement like that registered by a Fourier transform spectrometer can improve the SNR, compared to that of a scanning grating spectrometer, of the order of the square root of m, where m is the number of points in the spectrum.

– Jacquinot [JAC 48, JAC 54a, JAC 54b, JAC 60] on the optical throughput advantage or the Jacquinot advantage, which is linked to the intrinsic brightness of interferometers. An interferometer transmits the whole IR radiation that travels through the sample to the detection system. The circular apertures of the interferometer do not limit the illumination of the sample, unlike the slits in a grating spectrometer, which are required for a good resolution. Indeed, the finer the slit, the better the resolution, but in return, IR light is attenuated. The advantage of a Fourier transform spectrometer differs depending on wave number and resolution.

– J. Connes and P. Connes [CON 61a, CON 61b, CON 61c, CON 61d, CON 66] on the advantage of precise sampling through the interference fringes of a laser source, allowing the continuous recording of the measured spectrum; this technique can be used to precisely determine the optical path difference and also the data digitization during the interferogram acquisition. It is important to note that prior to the availability of the first gas lasers, P. Connes used a monochromatic cadmium lamp beam propagating through the interferometer, along the same path as the primary sample beam.

– Finally, Cooley–Tuckey [COO 65] on how Cooley–Tuckey fast Fourier transform (FFT) algorithm can be used to numerically obtain the inverse Fourier transform of the recorded interferogram, taking into account the constraints related to the instrumental line shape, apodization and optimum sampling interval, thanks to the works of J. Connes [CON 61]. The term Fourier transform infrared spectroscopy originated in this mathematical processing required for the conversion of interferogram data into the line spectrum.

FTIR spectrometer is a commonly used term nowadays. This technique is sometimes divided into two phases: the first one involves the recording of an IR spectrum of a sample as an interferogram, and the second one, the IR spectrum calculation by Fourier transform of the interferogram. The commercial brands of instruments such as Brucker, Bomem or Nicolet record the interferogram in numerical form in a file and then the corresponding spectra can be displayed on a screen after numerical Fourier transform by FFT.

1.2.1. *Principle of IR spectrum acquisition by interferometry*

[DAH 21] gives a description of a homodyne monochromatic interferometer using a laser as the source of monochromatic light of wavelength λ. It is made up of a fixed beamsplitter and a compensator, parallel to each other (Figure 1.1). After traveling through the beamsplitter–compensator set, the light beam splits into two paths (r_1 and r_2) and is then reflected by two parallel mirrors, a fixed one denoted by M_1 and a mobile one, denoted by M_2 (Figure 1.1). It can be noted that the rays reflected by M_2 travel through the beamsplitter twice, while those reflected by M_1 go through the beamsplitter once, leading to a phase shift. The compensator thus compensates and symmetrizes the optical paths in the two Michelson arms.

The beam recombined in the beamsplitter–compensator set generates interference fringes on the detector. These are constructive or destructive interference patterns, depending on the path difference Δx between the two rays, depending on the relative position of the two mirrors M_1 and M_2. The intensity can be written as a function of the electrical field E_0 of the radiation, which is as follows:

$$\frac{I(\Delta x)}{\varepsilon_0 c} = \frac{1}{2}\left|\vec{E}_0\right|^2 + \left|\vec{E}_0\right|^2 \cos\left(\frac{2\pi}{\lambda} r_2 - \frac{2\pi}{\lambda} r_1\right) = \frac{1}{2} I_0(\sigma)(1 + \cos(2\pi\sigma n(\Delta x))) \qquad [1.12]$$

where c is the speed of light and ε_0 is the vacuum permittivity.

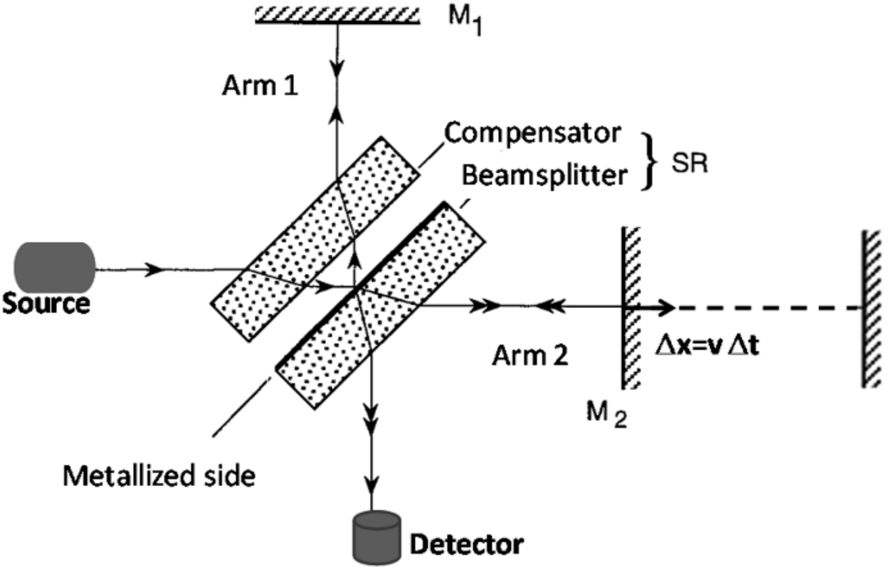

Figure 1.1. *Interferometer diagram. For a color version of this figure, see www.iste.co.uk/dahoo/infrared2.zip*

Interference fringes are formed in the observation plane, coinciding with the detector surface. When the mobile mirror moves, they are transformed into a modulated electric signal that follows the light intensity variations. This signal is directed towards a counter that counts the number of displayed fringes. A fringe is a complete cycle in the variation of light intensity, which passes periodically from a maximum value to zero and then to a maximum value. Each cycle corresponds to a displacement such that $\sigma n\Delta x = 2$. If the path difference Δx corresponding to a cycle and the index n of the surrounding medium are known, the wave number σ or the wavelength λ can be deduced. Conversely, if n and λ are known, Δx can be deduced.

In an interferometer used for studying the spectrum of molecules absorbing light in the IR range, the source used emits a complex polychromatic radiation. If the incident monochromatic flux of wave number σ is denoted by $\phi(\sigma)$, then for a path difference $\Delta = n\Delta x$, the expression of the emergent flux is written as:

$$\phi(\Delta) = \frac{1}{2}\int_0^{\infty} \phi(\sigma)(1 + \cos(2\pi\sigma\Delta))d\sigma \qquad [1.13]$$

The variable part $\phi(\Delta) = \frac{1}{2}\int_0^\infty \phi(\sigma)(\cos(2\pi\sigma\Delta)d\sigma$ is referred to as the interferogram. In practice, it is the intensity $I(\Delta)$ that is recorded as a function of the path difference Δ, and whose expression is given by:

$$I(\Delta) = \int_0^\infty B(\sigma)\cos(2\pi\sigma\Delta)d\sigma \qquad [1.14]$$

where $B(\sigma)$ is the recorded spectrum.

For a given path difference, the detector receives a signal that contains all of the information about the spectrum, and the energy corresponding to each spectral element is integrated over the measurement time *T*. In the classical spectrographs or spectrometers, the energy corresponding to the same spectral element is integrated over the time interval *T*/*N* of the measurement, where *N* represents the number of spectral elements received by the detector.

Then, the spectrum is reconstructed by inversion using a Fourier transform such that:

$$B(\sigma) = \int_0^\infty I(\Delta)\cos(2\pi\sigma\Delta)d\Delta \qquad [1.15]$$

The calculation of $B(\sigma)$ with formula [1.15] implies that $I(\Delta)$ is known over all of the values ranging between 0 and infinity. In practice, the maximum path difference is fixed at a value Δ_M that is the limit of the displacement of the mobile mirror. Under these conditions, the product of $I(\Delta)$ by the rectangular function $H(\Delta) = \mathrm{rect}(\Delta/2\Delta_M)$ is retrieved instead. Consequently, the calculation of $B(\sigma)$ actually corresponds to that of the Fourier transform of the product $I(\Delta)\mathrm{x}H(\Delta)$, or the convolution product $B(\sigma)*A(\sigma)$, where $A(\sigma)$ is the apparatus function of the interferometer, which depends on the maximum possible path difference. It is important to note that the higher this value, the narrower the apparatus function.

1.2.2. *Design and operation of a long path difference interferometer*

This section mainly describes the optical and electronic techniques developed for the operation of an interferometer over a long path difference. In order to guarantee measurement stability and increase the SNR over a very long distance corresponding to a path difference of 14 m, the step-by-step interferometer, operating in continuous regime, built by the molecular spectronomy laboratory, is based on the principle of Connes interferometer [CON 66, PIN 67, CON 75, PLA 86].

It features a device composed of a concave mirror and a plane mirror placed in its focus (cat's eye) [CUI 67], so that the ray reflected by the mobile mirror remains parallel to the ray incident on the fixed mirror throughout the displacement path, and can also be modulated in position by a piezoelectric ceramics support.

The path difference is measured using a He–Ne laser stabilized in the central dip of its gain profile ("Lamb dip" or saturated absorption). The monochromatic laser beam of wavelength λ_0 is concentric to the beam of the polychromatic IR source illuminating the sample being studied.

The two beams at the output of the beamsplitter–compensator device each travel through a quarter-wave plate oriented so that each beam is circularly (one right-handed and the other left-handed) polarized [DAH 21]. Then, when these beams recombine, a linearly polarized wave is obtained, whose azimuth depends on the path difference. The linear wave is then split into two beams and sent to two photomultipliers through $\pi/4$ polarizers. The signals at the output of the photomultipliers measure the azimuth of the linearly polarized wave, hence the rotation position of this polarization, which depends algebraically on the path difference.

To achieve the step-by-step mode, the path difference is modulated at a frequency f_0 = 100 kHz by applying a sinusoidal voltage to piezo-electric ceramics glued on the mirror of one of the cat's eyes. Thanks to this modulation, a detection synchronous with the position of this mirror is achieved. The signals at the output of the photomultipliers are directed towards a broad band filter centered on the frequency f_0 and with a very steep slope to dampen the harmonics in the output signals. These signals are processed and put in phase quadrature at the frequency f_0 and are then added to obtain a signal of constant amplitude, whose phase depends on the path difference Δ. Since the carriage of the mobile part of the interferometer moves at constant speed, the frequency of the detected signal varies depending on the direction of motion. This property is used to precisely localize the position of the carriage. The signal of constant amplitude and variable phase is applied to a logical circuit that sends a pulse at each zero crossing. These pulses are then subtracted from pulses synchronous with the pulses of the signal at f_0. The adder output represents the error signal in digital form. The response range is ± 20 µm. This error signal is sent through a control loop after passage through a DAC (digital to analogue converter). The path difference variations are obtained by sending pulses to the adder. Each pulse creates a path difference of $\lambda_0/8$, where λ_0 is the wavelength of the He–Ne laser serving as reference.

An optical system composed of mirrors allowed the use of absorption cells of various lengths and designs (multiple reflection cells of paths ranging between 5 m and 40 m, or cells of lengths below 1 m). The adjustment of the optical throughput was defined by the entrance aperture of the interferometer, among which are the entrance aperture of diameter 10 mm, the image of the beamsplitter on the collimator of diameter 31 mm and the distance between the entrance aperture and the beamsplitter image of 754 mm.

The internal modulation of the path difference eliminates the continuous background accompanying the interferogram. For a given value Δ_0 of the path difference, the value measured on the interferogram $I(\Delta_0)$ is obtained by the synchronous detection of the signal detected in the observation plane. In the case of square wave modulation, $I(\Delta_0)$ is written as:

$$I(\Delta_0) = \int_0^\infty B(\sigma) sin\pi\sigma\Delta_M \sin(2\pi\sigma\Delta_0) d\sigma \qquad [1.16]$$

where Δ_M is the amplitude of internal modulation.

By choosing $\sigma\Delta_M = 1/2$, the reception system records the derivative of the interferogram, which is more interesting for the search of the zero path difference from which each recording starts. Moreover, with the spectrum being bounded, the application of Shannon's theorem makes it possible to determine the optimum sampling interval that depends on the studied spectral width. The Cooley–Tuckey FFT algorithm is then applied to numerical data in order to calculate the sample spectrum from the interferogram.

The width at mid-height of the apparatus function is imposed by the maximal path difference of the interferometer, Δ_{Max} =14 m, so that $\Delta\sigma \cong 1/(\beta\Delta_{Max})$, where the value of coefficient β depends on the apodization functions and varies between 1.2 and 1.8. The maximum resolution power is given by $R \cong \sigma / \Delta\sigma \cong \Delta_{Max} / \lambda$. For $\lambda = 14$ µm, $R = 10^6$.

Data acquisition was performed using the microcomputer MICRAL from the R2E company, according to a procedure described in [DAH 89], which was developed during supervised training in a research laboratory and proposed to engineering schools. Anecdotally, it is important to note that MICRAL is the first microcomputer whose invention was attributed to F. Grenelle in 1998, who thus promoted the use of the INTEL 8008 microprocessor. The development of MICRAL originated in a call for projects launched by INRA (French National Institute for Agricultural Research) in 1972, the purpose of which was to control the watering of fields, depending on ambient temperature and humidity conditions. The paradigm of Artificial Intelligence had not yet been formulated in those times.

The program written in low level assembly language was used to manage the interruptions between the acquisition device of the interferometer and MICRAL, data acquisition (16 bits per point of the interferogram), the formatting of data coded in hexadecimal ASCII, its visualization on the screen and its writing on a floppy disk by a block of 256 measurements, the commands for the management of the dialogue between the interferometer and MICRAL and the management of floppy disk writing.

The communication between the interferometer and MICRAL allows the management of a step-by-step operation mode, by controlling the acquisition of data from the MICRAL using a read command by the micro-processor. It also permits a continuous operation mode by which data acquisition was automatically achieved at the scanning rate imposed by the mobile carriage of the interferometer, moving from the zeroth path difference to the desired maximal distance from a read command, satisfying Shannon's criterion of non-overlapping spectra. The acquisition speed was generally 100 measurements per second, and an interruption made it possible to write all 256 measurements on a data block. It is important to note that the correction of the wave number at the top of the lines, which takes into account the variation of the air index between the visible and the 10 μm region, was determined by the formula:

$$\sigma_0 = (1 + 0.00034)\sigma + 0.0014 \qquad [1.17]$$

The recording characteristics depend on the spectral range of the measurements. In the spectral range from 930 to 1,170 cm^{-1}, a HgCdTe photovoltaic detector was used, cooled with liquid nitrogen. The sampling interval was fixed at $206\lambda_0/8$, the internal modulation amplitude at $62\lambda_0/8$, and the frequency of synchronous detection at 377 Hz. In the spectral range from 718 to 1,077 cm^{-1}, a GeHg detector was used, cooled with liquid helium, featuring a wide-band cold filter (77 K) cutting at 1,300 cm^{-1}. The sampling interval was fixed at $176\lambda_0/8$, the amplitude of the internal modulation at $60\lambda_0/8$ and the frequency of synchronous detection at 328 Hz. For a cold filter cutting at 970 cm^{-1}, the sampling interval was fixed at $184\lambda_0/8$, the amplitude of internal modulation at $62\lambda_0/8$ and the frequency of synchronous detection at 332 Hz.

1.2.3. *FTIR absorption spectroscopy in matrices*

The matrix technique consists of the isolation of neutral species, pairs of ions or radicals in inert solids at low temperatures, for their study. It can be used in particular, for the study of unstable molecular species. Applied for the first time by Lewis [LEW 41] who studied the phosphorescence of aromatic molecules suspended in a rigid vitreous medium at low temperature, it was revisited a dozen years later by

Porter [POR 50, POR 68] and Pimentel [DOW 54, PIM 60, PIM 62, PIM 63]. Argon and nitrogen are used as matrices to isolate molecules in order to obtain free radicals by photolysis, which can be studied using IR spectroscopy. Pimentel and his collaborators had a huge contribution to the development of this technique afterwards. The matrix technique involves the isolation of neutral species, pairs of ions or radicals in inert solids at low temperatures, and their subsequent study by frequency- and time-resolved spectroscopy. The research on the absorption spectroscopy of molecular chemical species isolated in an inert matrix requires a spectrometer. At the beginning of the 1990s, in the group led by L. Abouaf-Marguin and L. Schriver-Mazuoli at the Laboratory of Molecular Physics and Applications of Sorbonne University in Paris (formerly Pierre and Marie Curie University) [BRO 93, ABD 93, LUG 94, DES 94, JAS 95, RAD 95, DAH 97, BAH 97, HAL 98, CHA 00a, CHA 01, COA 03], a Fourier transform spectrometer (Bruker IFS 113V) was used to record the IR absorption spectra for the spectroscopic study of molecules trapped in an inert matrix. The recorded spectra can also be used to control the preparation of the crystalline sample on the sample holder surface inside a cryostat.

The experimental setup was used for frequency-resolved and time-resolved spectroscopic studies [ABO 73, DUB 75, GAU 80, BOI 85, ZON 86]. Figure 1.2 presents an example of the experimental setup. The apparatus used for preparing the gas mixture and then the crystalline sample during deposition is independent from the excitation and analysis system. It includes a cryogenic set for the fabrication of the crystalline sample (Figure 1.3) from a mixture of the matrix and molecular species to be studied in the gas phase, prepared in a chemical apparatus under secondary vacuum.

A commercial cryostat equipped with a reflective sample holder can be used to condense the gas mixture on a metallic support cooled with liquid helium. The sample holder consists of the polished and gilded side of a copper block covered with a gold layer, which also serves as a mirror. The spectroscopic study is conducted by reflection on this mirror, with the beam traveling through the sample twice. A control system composed of a diode and a logical set is used to reach the desired temperature. Probes embedded in the sample holder are used to measure its temperature: a platinum resistance for temperatures above 30 K and a carbon resistance for temperatures ranging between 4.2 and 30 K. In the setup used, the platinum is located above the sample holder block, and the carbon is lower, in the block. A diode is located at the level of the vaporization chamber and of a heating resistor. The base of the cryostat has three windows in KBr, allowing the passage, on the one hand, of the IR beam, and, on the other hand, of the pump pulse and the observation of fluorescence for the vibrational relaxation experiments. The set is maintained under secondary vacuum (10^{-5} Torr).

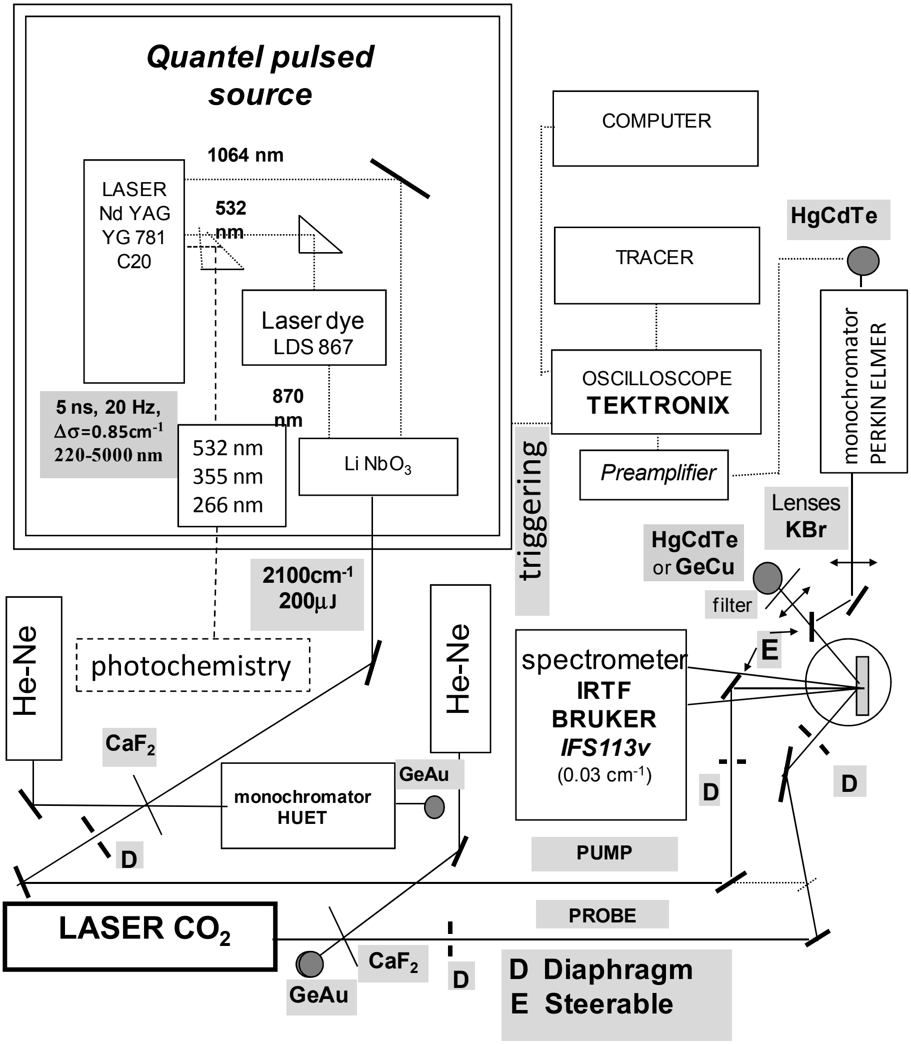

Figure 1.2. *Experimental setup for laser spectroscopy: induced fluorescence and IR–IR double resonance*

The spectroscopic study is conducted using a Fourier transform IR spectrometer made by Bruker (IFS 113V), operating under primary vacuum. The set composed of a Michelson interferometer and a He–Ne laser embedded in the interferometric block allows the sampling of the IR interferogram. The spectra are recorded between 500 and 4,000 cm^{-1} with a resolution of 0.5 cm^{-1} or of 0.15 cm^{-1}, depending on the sample, using a DTGS detector operating at ambient temperature. The interferometer embedded software is operated to control the linearity of the sample deposit and the analysis of the IR absorption spectra (Figure 1.4).

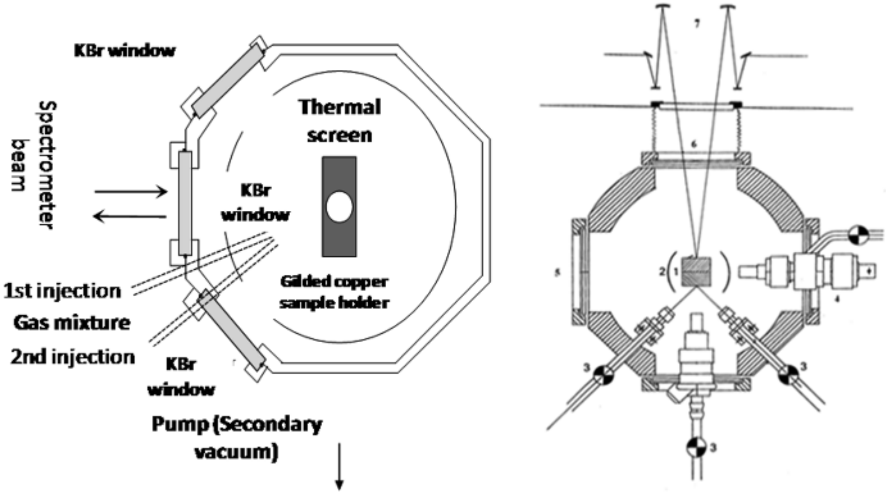

Figure 1.3. *Experimental setup of the cryostat head*

A characteristic of this device is that the beamsplitter–compensator support continuously moves on an air cushion. A maximum resolution without an apodization of 0.03 cm^{-1} is reached for a path that is half of the one traveled by the mobile mirror of a classical interferometer. The duration of spectrum acquisition is thus reduced. The maximum path difference is 32 cm. Conducting fine spectroscopic studies sometimes requires a reduction of the spectral region to be investigated, by means of an interchangeable beam splitter. In medium infrared (MIR), a potassium bromide (KBr) plate containing a deposit of germanium is used as the beamsplitter. For far IR, a mylar sheet is used for the spectroscopic study in the region of vibrational mode ν_2 of molecules N_2O and CO_2.

The beam entrance flux is controlled by an adjustable aperture located at the exit of the compartment containing the IR source (Globar: silicon spiral heated at 1,200 K). The light is sent on the sample holder mirror of the cryostat and is then reflected towards an MCT detector cooled with liquid nitrogen for rapid acquisitions (100 scans in 10 minutes). The quantitative measurements are conducted with a DTGS detector operating at ambient temperature, with a higher linearity than MCT, but at a slower rate (100 scans in 60 minutes). The diameter of this aperture at the source exit must be compatible with the desired resolution. Therefore, a resolution of 0.5 cm^{-1} corresponds to a wide open aperture (10 mm). On the other hand, for a resolution of 0.15 cm^{-1}, the diameter must be reduced to 5 mm. In this case, the energy received by the detector is lower and may prove insufficient for analyzing the spectra of certain samples. The lack of transmitted energy can be critical, as with the xenon and krypton matrices. These two matrices are very scattered and reduce the transmitted intensity of the IR beam. For thick deposits, the SNR is then too low, and the resolution must be reduced to 0.5 cm^{-1}.

The more rapid MCT detector, cooled with liquid nitrogen, can be used for spectra acquisition with a higher scanning speed. However, at the same resolution, the SNR is not better, since in order to avoid saturation of MCT, which is more sensitive than DTGS, the globar source flux on the detector must be limited. On the other hand, resolution can be increased for the studies of thick deposits.

The spectrometer is controlled by a computer that exclusively uses Bruker software. Depending on the studies to be conducted, the operating parameters such as scanning speed, number of scans, resolution, diameter of the source diaphragm aperture, beamsplitter, detector, compartment (backside for our experiments) and electronic filters to reduce the number of points to be taken during the recording of the interferogram, are input as data and are then validated by the program prior to spectra acquisition. The Fourier transform of the interferogram is then calculated using an apodization function proposed by Bruker software. It is important to note that, depending on the desired resolution, a set of graphs can be used to make the best choice of electronic filters, scanning speed and source diaphragm aperture.

The Bruker interferometer is placed in front of the central window of the cryostat (see Figure 1.4). It is made up of a beam extractor, whose design allows the recording of spectra by reflection at 30 cm from the interferometer exit, thanks to an optimization of the position of its mirrors. The IR beam travels in the air over a distance of several centimeters between the two devices. In order to avoid absorption by the carbon dioxide or water vapor molecules in the air, this volume is flushed with nitrogen gas. Before deposit, two spectra without samples are recorded at 5 K with resolutions of 0.5 cm^{-1} and 0.15 cm^{-1}. They serve as references to calculate absorbance spectra, which are obtained by taking the logarithm of the ratio of the reference spectrum to the sample spectrum. When a sample is deposited, a preliminary spectroscopic study is simultaneously conducted to make sure that the optical density in the absorption spectra increases linearly, depending on the number of torrs deposited.

The space available between the window of the cryostat and the spectrometer allows the positioning of optical devices for time-resolved spectroscopy studies. All of the optical paths inside the spectrometer are pumped under permanent vacuum. Before the deposition, a reference spectrum without a sample is acquired at a resolution of 0.15 cm^{-1}, at a temperature of 5 K. The spectrum of the sample is calculated in absorbance form by taking the logarithm of the ratio of reference spectrum and the spectrum of the sample.

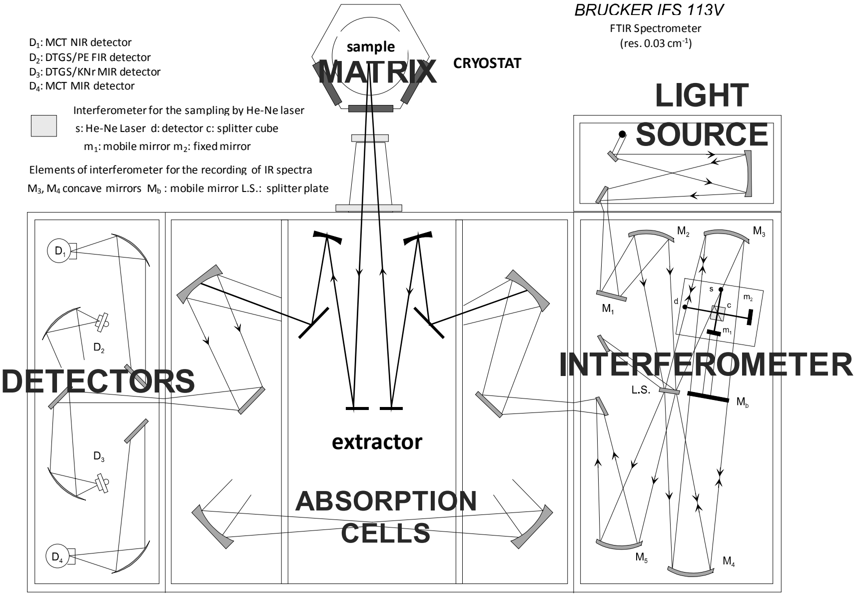

Figure 1.4. *FTIR spectrometer and experimental setup. For a color version of this figure, see www.iste.co.uk/dahoo/infrared2.zip*

Among the results obtained with this experimental setup, it is important to highlight the observation of simple and double substitution sites for the trapping of the O_3 molecule in rare gas matrices (Figure 1.5) [BRO 93], and also the presence of two CO_2 trapping sites and the degeneracy lifting of mode ν_2 of CO_2 in a double substitution site, termed as an unstable site (Figure 1.6) [DAH 99, CHA 00c], and of the presence of only one trapping site for the N_2O molecule, a double substitution site that lifts the degeneracy of mode ν_2 (Figure 1.7) [CHA 00d].

The spectroscopic studies conducted with this experimental device are explained in the following references: [BRO 93, ABD 93, LUG 94, DES 94, JAS 95, RAD 95, DAH 96, BAH 97, HAL 98, CHA 00a, CHA 01, COA 03].

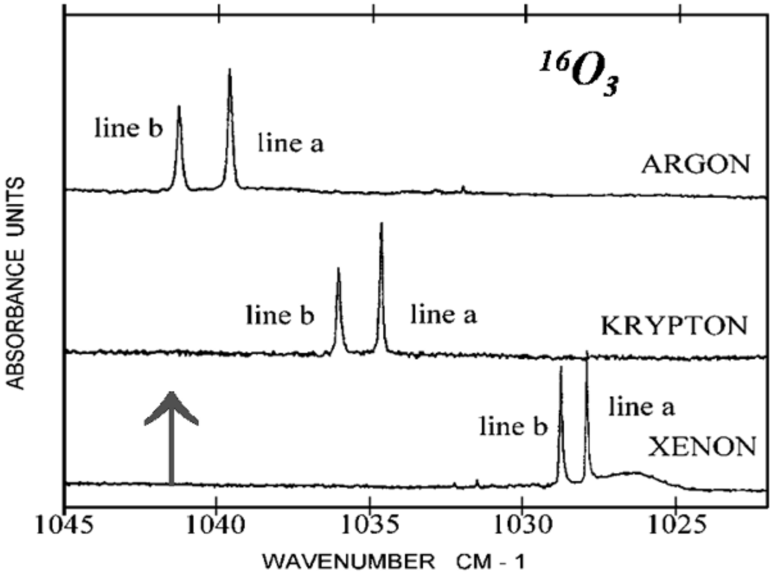

Figure 1.5. *O_3 region ν_3: (a) HF double site and (b) BF simple site (gas: 1042.08 cm^{-1}). For a color version of this figure, see www.iste.co.uk/dahoo/infrared2.zip*

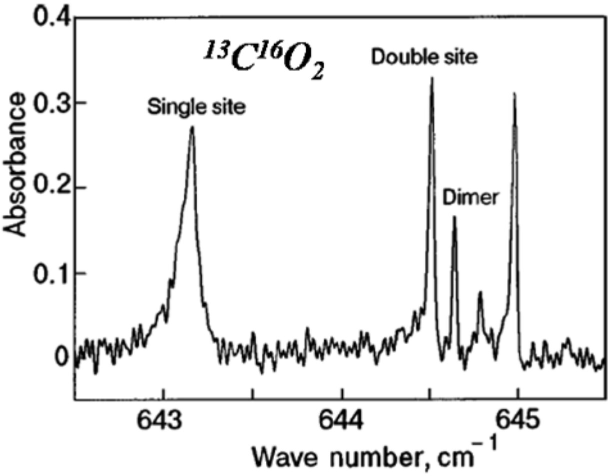

Figure 1.6. *CO_2 region ν_2: (a) BF stable site and (b) HF unstable site (gas: 648.5 cm^{-1})*

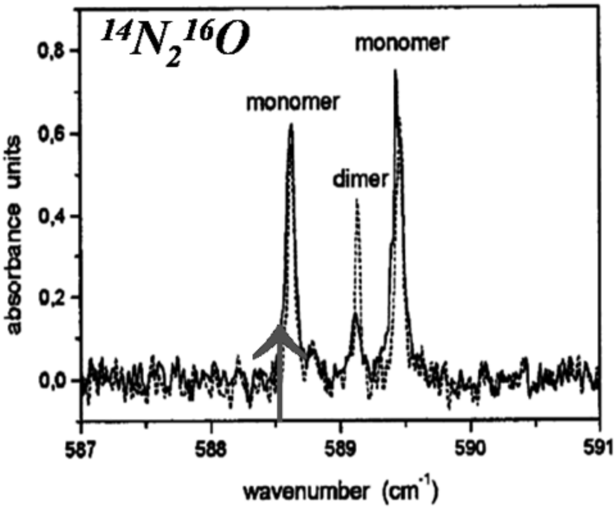

Figure 1.7. *N_2O region ν_2: double site (gas: 588.77 cm^{-1})*

1.2.4. *LIF and DR IR–IR spectroscopies in matrices*

The time-resolved laser spectroscopy conducted with this experimental device was described in Chapter 7 of [DAH 16]. The experimental techniques of laser-induced fluorescence and double resonance (LIF and DR) originate in the works of Kastler and Brossel [BRO 49] for DR, and Kastler [KAS 50] for optical pumping. They were applied within the framework of optical detection methods of magnetic resonance that can be used for the study of atomic level structures. The progress of time-resolved laser spectroscopy techniques, LIF and DR (LIF for Laser-Induced Fluorescence and DR for Double Resonance), unfolded in parallel with the development of lasers. Based on the theoretical model of Schawlow and Townes [SCH 58] showing the feasibility of IR and optical lasers, the development of the first lasers, the pulsed ruby laser, at 3.39 μm, invented by Maiman in 1960 [MAI 60] and the continuous He–Ne gas laser, at 1.15 μm, invented by Javan *et al.* [JAV 61] in 1961, revolutionized LIF spectroscopy. Indeed, the coherent light of lasers is better adapted to the LIF technique than the light emitted by classical sources.

The first works in this field were conducted by the inventors of laser sources themselves. Javan *et al.* studied the vibrational relaxation of CO_2 using the LIF technique in 1966 [HOC 66] and Schawlow *et al.* studied the laser-induced selective photo-catalysis of bromine [TIF 67] using a laser source to excite the bromine molecules in the gas phase up to the first quantum bound states, close to the continuum of dissociation in 1967. The paths opened up by the intense monochromatic laser sources (high power per unit surface) for the studies of photochemistry, molecular spectroscopy or energy transfers by lasers were underlined in the article [TAN 68]. A review of the LIF technique is given in [ZAR 12]. In France, time-resolved laser spectroscopy on molecular systems trapped in matrices was developed by Abouaf-Marguin, after post-doctoral studies conducted in the United States, under the coordination of Jacox [MIL 67, ABO 77] at the Laboratory for Molecular Photo-Physics at Paris Saclay University (formerly Paris Sud University) [ABO 73, DUB 75, GAU 80, BOI 85, ZON 86].

Laser-induced fluorescence (LIF) spectroscopy is the process by which a molecule trapped in an inert matrix is excited by a laser beam, and the light subsequently emitted by the excited molecule is detected. With respect to absorption spectroscopy, LIF detection features a better detection sensitivity, as the signal is observed against a dark background, which limits the ambient noise. Since fluorescence is emitted in all directions, it can be collected under various angles with respect to the incident laser beam, which makes it possible to obtain two- and three-dimensional images. Moreover, by using a monochromator for frequency-resolved fluorescence, it is also possible to determine the transitions from the excited state to various lower levels of the excited molecule. The time delay between the events related to excitation and detection makes it possible to study the processes through which the excited molecule returns to its initial state in the time interval between the onset of the laser excitation and that of the fluorescence detection.

The experimental setup presented in Figure 1.2 was used to determine the effect of an inert matrix on the atmospheric molecules trapped in substitution sites by time-resolved spectroscopy. The laser-induced fluorescence and IR–IR double resonance experiments conducted on O_3, CO_2 and N_2O involved a set of lasers (pump laser) (Figure 1.8) (YAG, laser dye, doubling (visible), tripling, quadrupling, quintupling (UV) and mixer (IR) crystals), completed by a continuous CO_2 laser (probe laser) and a system composed of a cryostat and Brucker IFS 133v interferometer, to prepare and characterize the samples.

A flash lamp is used for optical pumping and achieving the energy level population inversion in the YAG rod. The rod, which is the active medium, is a yttrium–aluminum–garnet (YAG) crystal weakly doped (0.1%) with neodymium (Nd^{3+}) ions. The active medium emits a fluorescence on the $4F_{3/2}$ -$4I_{11/2}$ transition line at 1,064 nm of Nd^{3+} ions. The high power flash lamp is composed of a cylinder located at one of the foci of a cylindro-elliptical mirror, while the YAG rod is located in the other focus. The rod and the lamp are thermostatically regulated by controlled water circulation. A dichroic crystal is used for the second harmonic generation at 532 nm, a tripling crystal gives the 355 nm line and finally a quadrupling crystal gives the 266 nm line. In order to increase population inversion, the laser operates under switched mode by a delay in the input of laser oscillations, with respect to the lamp flash. The switched mode of the laser is controlled by a Pockels cell and by a polarizer, making it possible to reach opening times of nearly 5 ns with a frequency of 20 Hz.

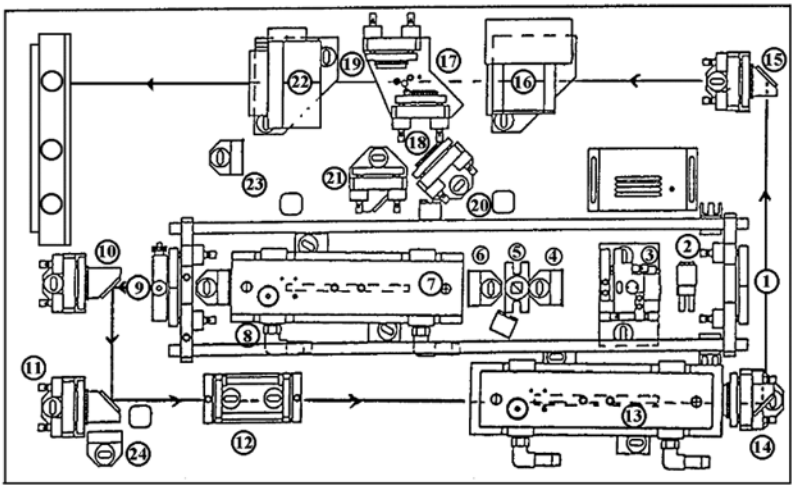

Figure 1.8. *Nd-Yag laser: (1) cavity bottom mirror (Rmax = 1,064 nm), (2) shutter, (3) Pockels cell, (4), (6), (8), (23) quarter wave plate, (5) horizontal polarizer (GLAN), (7) laser head, (9) output mirror (cavity bottom) of variable reflectivity, (10), (11), (14), (15), (19), (21) reflective mirrors Rmax = 1,064 nm, (12) telescope, (13) amplifier, (16) doubling crystal, (17) stage with two oscillating mirrors, of which (18) one mirror with Rmax = 532 nm, Tmax = 1,064 nm and (19) one mirror with Rmax = 532 nm, (20) reflective mirrors with Rmax = 532 nm and (22) tripling or quadrupling crystal (24) beam blocker*

The IR module of the dye laser set has three core elements: the frequency doubled YAG laser, a dye laser and a mixer crystal to produce mid-IR (Figure 1.9).

Its operation relies on these three devices. Laser pulses are generated by a flash pumped YAG rod, whose frequency is then doubled through a doubling crystal. The dye laser involves an oscillating cavity and two amplifying cells containing a dye solution (LDS 867) pumped by the 532 nm radiation. The set emits IR pulses (35 mJ/pulse) at about 870 nm. The frequency calibration is determined by the position of a toothed wheel that rotates a grating (2,400 traits/mm) in the dye oscillator cavity. Wheel rotation can be manually controlled by an operating wheel, or automatically controlled by a control unit or a computer. This control system can be used to precisely adjust the frequency (0.02 cm^{-1}). The spectral width of the pulse can be reduced from 2.5 cm^{-1} to 0.8 cm^{-1} by means of a beam expander located in the cavity of the oscillator. Finally, a $LiNbO_3$ crystal placed in a last module generates the IR radiation by parametric conversion. The beam issued by the dye laser (35 mJ/pulse) and that of the residual YAG laser (40 mJ/pulse) cross the crystal and intersect in its center. A third wave resulting from the subtraction of frequencies of the two incident beams can be available at the exit. The efficiency of this nonlinear effect depends on the geometrical phase matching of the wave vectors of the YAG and dye beams through the crystal. Each frequency of the dye is related to a specific inclination of the crystal. The orientation of the latter, placed on a holder that can be adjusted by an operating wheel, must be modified at each frequency change, in order to maintain the IR laser intensity. In an optimized configuration, the crystal provides pulses of about 200 µJ with the same spectral and temporal qualities as the pulse of the dye ($\Delta\nu = 0.8\ cm^{-1}$ and $\tau = 5$ ns). The frequency of the emitted radiation ranges between 2 µm and 4.8 µm, depending on the frequency of the dye. It is used around 2,100 cm^{-1} in resonance with the transition $\nu_1+\nu_3$ of the ozone in matrices for laser spectroscopy.

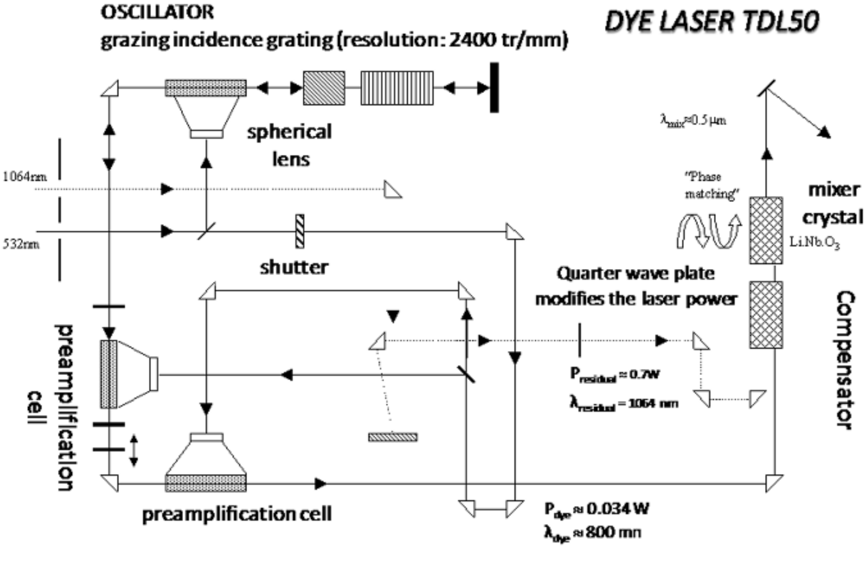

Figure 1.9. *Dye laser, cavities, optical elements and mixer crystal* $LiNbO_3$

The results are published in the following references: [JAS 94, JAS 95, BER 96, DAH 97, DAH 98, JAS 98, CHA 00a, CHA 00b, CHA 00c, CHA 02, VAS 03]. For example, the global fluorescence observed for two trapping sites of CO_2 in the argon matrix (Figure 1.10(a) and (b)) is more chaotic for the unstable site, with signals constituted of short (one at 10 μm and two at 16 μm) and long (one at 16 μm) component superpositions in the time domain.

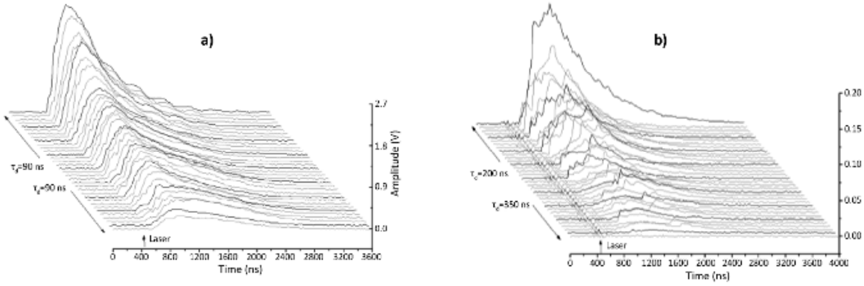

Figure 1.10. *Global fluorescence: (a) stable site and (b) unstable site, Ar/$^{13}CO_2$ = 2 000, T = 5 K [CHA 00a, DAH 16]*

Chapter 7 of [DAH 16] presents a summary of the time-resolved spectra that were observed. Fluorescence was observed after excitation in the IR range in the region around 4.5 μm, of the vibrational mode $\nu_1+\nu_3$ of the fundamental electronic state of $^{16}O_3$ [JAS 94, JAS 95, DAH 97, JAS 98, CHA 00b] and of the vibrational mode ν_3 of $^{13}CO_2$ [BER 96, DAH 97, CHA 98, CHA 00a, CHA 00c, CHA 02, VAS 03] and $^{14}N_2O$ [BER 96, DAH 97, CHA 00b, CHA 02]. Fluorescence differs from the pump pulse by a temporal delay and a weaker intensity. Correlated with the absorption zone, it fully disappears if laser frequency shifts outside the range. Its intensity is optimized by shifting the laser impact on the sample.

The results of the application of the IR–IR double resonance technique are essentially related to the studies conducted with the CO_2 probe laser on ozone in GR and nitrogen matrices [JAS 95, DAH 97, DAH 98]. A double resonance (DR) signal is characterized by three temporal parameters, τ_M, τ_R and τ. The time τ_M is the time for the signal to reach the maximum and corresponds to the mean duration of depopulation or repopulation of the initial level in the probed transition. The time τ_R is the characteristic rise time of the signal or decay time of the signal, and corresponds to the dynamics of interaction between the probe and the initial level. The decay time τ is usually determined by adjusting an exponential $s(t) = Aexp(-t/\tau)$ to a properly chosen portion of the signal. It is sometimes necessary to use two exponentials for the adjustment, by taking $s(t) = A_1\ exp(-t/\tau_1)+A_2\ exp(-t/\tau_2)$ when two independent phenomena are juxtaposed. These times are associated with the return of the initial level to its initial population state.

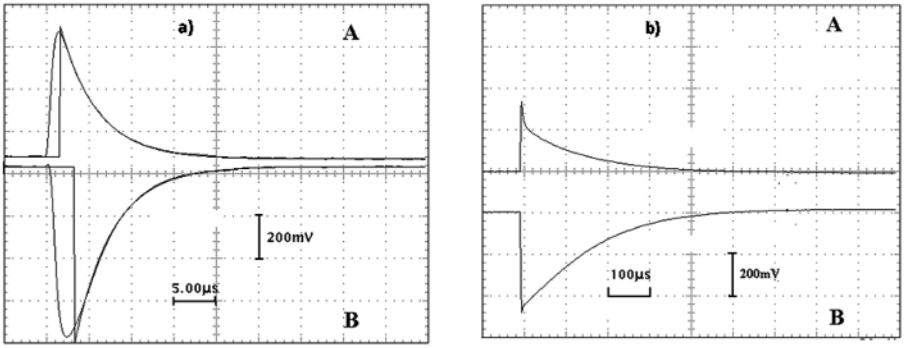

Figure 1.11. *Double resonance signals: (a) carried by the line P_{26} (A: 4.2 µs) and the line P_{42} (B: 4.1 µs) of the CO_2 laser ($O_3/Ar = 1/2\,000$, thickness: 110 mm); (b) superimposed probe (P_{26}) and pump (A) and probe (P_{26}) and pump laterally shifted (B) [JAS 95, DAH 97, DAH 16]*

A signal, due to a thermal effect (Figure 1.11(b)) that occurs as soon as an excited molecule releases its energy to the environment, is generally superimposed to the DR signal, on a time scale that is above the measured times (τ_1 and τ_2). In order to analyze the DR signal on its time scale, the amplitude of the thermal signal must be negligible compared to that of the DR signal. A second type of thermal effect, (Figure 1.11(b)) known in laser theory as the lens effect, must also be minimized to correctly analyze the DR signal. This effect is manifested in the superposition of a second positive or negative signal, depending on the relative positions of the pump and probe beams. Its decay (or rise) occurs over the same time scale as the thermal signal of the first type. This effect can be minimized by adjusting the relative positions of the beams, so that the positive signal compensates the negative one.

1.3. Resonant cavity laser absorption spectroscopy

Resonant cavity laser absorption spectroscopy involves the use of a laser source and a resonant cavity composed of highly reflective mirrors, of reflectivity nearly equal to 1, for the study of molecules in the form of trace. It is important to note that as early as 1962, Kastler [KAS 62] suggested the use of a Fabry–Pérot cavity for measuring atomic absorption and emission.

It is a technique through which the absorption of a medium is measured after multiple passages in a laser cavity, which operates as a multiple reflection cell. It can be used for the study of weak absorptions that are due to chemical species in the form of traces, or to weak transitions. In practice, the laser cavity operates as a filter that fixes the (longitudinal or transverse) modes (see Chapter 6 of [DAH 16] or the references [SIE 86], [DEM 96] and [GRY 97]) of the laser and on which laser amplification can occur (the cavity length is assumed to be constant by a feedback control). The introduction of a spatial filter in the form of a variable aperture diaphragm can be used to select only the transverse mode TEM_{00}. In this case, if the broadening of the laser gain profile is inhomogeneous, there is a gain increase after each passage of the laser beam in the cavity, and for the longitudinal modes that are within the gain profile and coincide with the absorption lines of the absorbing medium, lines appear in the laser profile of saturated gain (Figure 1.12). Saturation occurs from a threshold defined as the equality between the pumping gains and the back-and-forth beam path in the cavity and the intracavity losses [SIE 86, DEM 96, GRY 97].

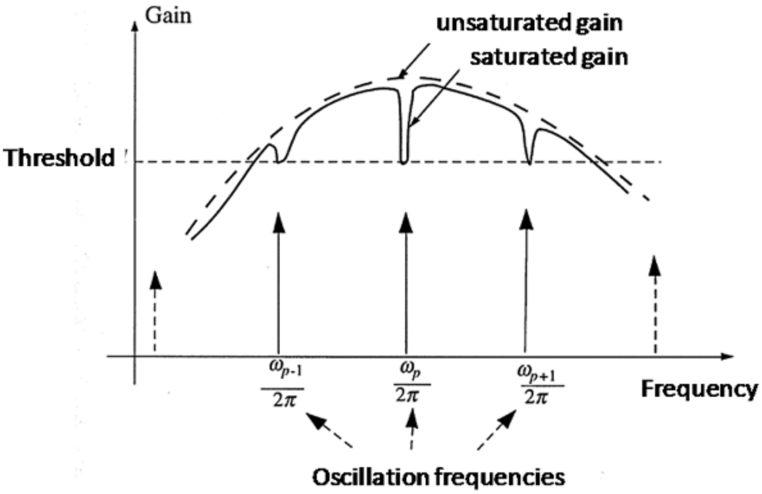

Figure 1.12. *Effect of gain saturation for an inhomogeneous widening: hole burning in the gain profile [DEM 96, GRY 97]*

With this technique, the absorbing medium is thus integrated in the source device in the laser cavity. The saturation of amplification or the decrease in gain when light intensity increases only affects the molecules of the amplifying medium, whose frequency is tuned on the active frequency. The simultaneous oscillation of all of the modes allowed by the threshold condition is observed. This phenomenon is possible because the broadening is inhomogeneous, which means that gain saturation only affects the molecules of the amplifier medium, whose frequency is tuned on the active frequency. At a given frequency, the laser effect does not affect the gain at another frequency. On the other hand, if the broadening is homogeneous, the response of each molecule is similarly affected by the gain saturation. The gain curve as a whole undergoes the effect of saturation.

Two techniques, namely the intracavity laser absorption spectroscopy (ICLAS) and the cavity ring-down spectroscopy (CRDS), are based on the multipassage intracavity absorption. The principle relies on the increase of the optical path, following multiple reflections of the laser beam on the mirrors in the cavity, and consequently, the absorption of these molecules. The finesse and the cavity gain are also parameters to be considered among the conditions allowing for the observation of the absorption of molecules inserted in the cavity. This technique follows the research works conducted on laser cavities, whose objective was to limit cavity losses in order to improve the laser output power and the gain profile. In this context, the objective was to improve the reflectivity of the cavity mirrors and to reduce the other sources of loss potentially due to impurities in the cavity.

In the ICLAS method, absorbing species are placed inside the cavity of a broad band laser. Because of the positive feedback mechanism of lasers, even tiny quantities of an absorber produce holes in the spectrum, where the laser exit is partially turned off. ICLAS was proposed in the early 1970s [PAK 70, PET 71, KEL 72, BEL 72]. It relies on the high sensitivity of a broad band multimode laser, compared to the selective losses inside the laser cavity.

For example, Pakhomycheva *et al.* [PAK 70] proposed that the line structure of the spectrum generated by a laser from an inhomogeneously broadened line is due to the high sensitivity of the laser spectrum to the presence of losses, depending on the frequency in the resonator. If the losses described by the following formula:

$$\frac{1}{T(\omega)} = \frac{1}{T_0} - \Delta(\frac{1}{T})\cos(\frac{\pi r \omega}{\Delta\omega}) \qquad [1.18]$$

are introduced into the laser cavity, the gain profile presents dips in the spectrum, with a relative intensity given by:

$$\frac{\Delta I}{I_0} = \frac{\Delta(1/T)}{1/T_0}\left(\frac{ST_0}{I_0} + \frac{I_0}{PT_0} e^{-(\frac{2\pi\gamma}{\Delta\omega})}\right) \qquad [1.19]$$

where ST_0, I_0 and P are, respectively, the spontaneous noise power, the generated power averaged over the frequency and the frequency density of the pumping power (power per unit frequency interval). The hypotheses leading to the expression of formula 1.19 are an infinite inhomogeneous width and a homogeneous broadening of the line profile characterized by a width γ. The proof of this effect and the validation of the equations used were studied with benzene and chlorobenzene, and also with the atmospheric molecules NH_3 and CH_4 inside a laser cavity.

Belikova *et al.* [BEL 72] described a method for the detection of weak absorption lines of gas, whose absorption coefficients are as low as 10^{-8} cm^{-1}. This method relies on the multiple passages of light through an absorbing substance during laser action. They show that the gain of a laser with an inhomogeneously broadened gain profile remains constant over the whole range of frequencies of coherent emission. This guarantees a high stability of the method. The theoretically predicted changes in the coherent emission spectra resulting from the presence of losses, depending on the frequency in the resonator, are confirmed by experimental results. The proposed method was used for the study of absorption spectra of ammonia, acetylene and water vapor in the spectral range of 1.06 µm.

Petersen *et al.* [PET 71] described a new technique developed to improve the detection of absorption spectra of weak absorbents. A laser with organic dye normally emits a continuous spectrum with a bandwidth from 2 nm to 10 nm. The effect of placing a sample of absorbing gas inside a dye laser cavity leads to an extinction of the laser at wavelengths where the absorption of the sample exceeds a minimal absorption threshold. The threshold of deactivation by absorption seems to be very low; an absorption of about 0.5% drives an alteration of the laser action at absorbing wavelengths and a shift of the laser emission towards wavelengths where the absorption is below the level of critical commutation. It is possible that the limits of detection of atoms and molecules by means of ICLAS, are by more than two orders of magnitude lower than those that can be reached by conventional absorption spectroscopy.

Keller *et al.* [KEL 72], in the same group as Petersen *et al.*, indicated that the insertion of samples in a broad band dye laser cavity improves the photographic detectability of absorption traces by about three orders of magnitude. Optical densities as low as 0.0004 were easily detected in a diluted solution of $Eu(NO_3)_3$ species. The technique by [PET 71] was modified, the bandwidth of the dye laser being reduced by the use of prisms. The wavelength of the narrow band is then used for a scanning through absorption. The modified technique allowed the detection of optical densities as low as 0.01. The solutions to the theoretical equations describing the two processes are in agreement with the experimental results and give an overview of the mechanism of the effect. The conclusion is that the measurements with broad band laser could be conducted in 100 ns or less, and that consequently, this technique should provide a powerful tool for the detection of short duration and very low concentration transients.

CRDS is a highly sensitive absorption method, based on the measurement of the decay profile of a laser pulse injected in an optical cavity. The length of the absorption path depends on the number of reflections required for the intensity to decrease by $1/e$. In the visible range, using the best available mirrors, the total length of the path can be about several dozen kilometers. Unlike the standard multiple passage absorption methods, as in the multiple reflection cells, the probed volume is limited to the cavity modes. Though described by Anderson *et al.* [AND 84], the proof of CRDS is attributed to O’Keefe and Deacon [OKE 88], who explicitly use the term CRDS to describe their invention. CRDS has since been used in many applications.

Anderson *et al*. [AND 84] described their invention as a reflectometer that can be used to measure the reflectivity of low-loss highly reflective mirror coatings and the transmission of low-loss antireflective coatings. The technique directly measures the intensity decay time of an optical cavity composed of low loss elements. They developed the theoretical framework of the instrument and discussed the conditions under which and extent to which the decay time represents a genuine measure of the mirror reflectivity. The instrument described provides a resolution of the decay time of 10 and shows a resolution of total loss of the cavity of 5 ppm.

O'Keefe and Deacon [OKE 84] developed the CRDS technique, which can be used to conduct measurements of optical absorption using a pulsed light source, which offers a far higher sensitivity than that obtained with continuous light sources. The technique relies on the measurement of the absorption rate, rather than of the absorption amplitude of a light pulse confined in a closed optical cavity. The decay in light intensity in the cavity is a simple exponential, with losses due to loss on the mirrors, broad band scattering (Rayleigh, Mie) and molecular absorption. The narrow band absorption spectra are recorded by scanning the output of a pulsed laser (that is injected in the optical cavity) by means of a resonant absorption. [OKE 84] prove the sensitivity of the technique by the measurement of several bands in the forbidden transition $b\Sigma_g^- - X\Sigma_g^-$ of very low intensity of the oxygen molecule in the gas phase. Absorption signals below one part per million are also detected.

1.3.1. *Intracavity laser absorption spectroscopy (ICLAS)*

The study of weak molecular transitions at high resolution can be conducted using the intracavity laser absorption spectroscopy (ICLAS) [STO 66] technique. This method relies on the high sensitivity of a broad spectral band multimode laser, in relation to the low intracavity laser absorptions, which are selective losses. The minimum detectable absorption coefficient is about 10^{-9} cm^{-1} for measurement times of several seconds. Typically, with the ICLAS technique, a substance is inserted in the laser cavity oscillating over a range of wavelengths. If the sample absorbs within the range of wavelengths emitted by the laser, the absorption characteristics affect the laser spectrum by an amount that is measurable. ICLAS is very sensitive, as it allows extremely long effective path lengths and high spectral resolution. The technique relies on the temporal dependence and the high sensitivity of a multimode laser, whose losses depend on the intracavity frequency when the spectral width of the absorbing species is greater than the spacing between modes and narrower than the gain profile.

Intracavity absorption in the spectrum of a laser with a homogeneously broadened gain profile is represented in a logarithmic scale by $N\sigma(\nu)\ ct_g = N\sigma(\nu)\ Leq$, where N is the density of absorbing species, $\sigma(\nu)$ is the effective absorption cross section, c is the speed of light and t_g is the generation time (the time between the onset of the laser emission and the observation time). The product ct_g can be defined as an equivalent absorption path Leq. The linear growth of the equivalent absorption path is limited by the spontaneous emission at a characteristic time $\tau \cong \langle M\rangle/\gamma$, where $\langle M\rangle$ is the average number of photons in the mode and γ is the intracavity loss rate. The characteristic time τ_{sp} expressed through the parameters of the cavity and of the active medium provides an estimate of the fundamental sensitivity limit for an intracavity spectrometer:

$$\tau_{sp} \cong \frac{(\eta-1)^2 w_0^4 L}{32\sigma_0^2 \Gamma^2 \tau^2 c^3 ln(R^{-1}(1-T_i)^{-2})} \qquad [1.20]$$

where L is the cavity length, w_0 is the laser beam radius inside the active medium, R and T_i are the output mirror reflectance and the intracavity losses, respectively, η is a pump power excess above the threshold, and σ_0, Γ and τ are the emission cross section, the gain linewidth and the fluorescence lifetime of the active medium, respectively. For a typical Ti:sapphire laser, this yields $\tau_{sp} \cong 0.7$ s, and $Leq \cong 210{,}000$ km! [KAC 94].

The very weak absorption lines of an absorber inside the cavity of a multimode laser can modify the laser spectrum and appear superimposed on the broader spectrum of the laser. This phenomenon is universal, meaning that any laser with a homogeneous gain profile (such as dye lasers, color center or Ti:sapphire) can be easily transformed into an ICLAS spectrometer [CAM 90]. This technique is very sensitive, as an equivalent absorption path up to a 100 kilometers can be reached. Consequently, a very low absorption coefficient can be detected, and it is proportional to the absorber density and to the line intensity. ICLAS was used to observe a weak absorption of NO_2 and CH_4, cooled in a supersonic jet through a slit. By using this method, the thermally congested spectrum of molecules is considerably simplified and the analysis becomes possible [CAM 91]. The major application domains of the ICLAS technique are the detection of low-density absorbers, the observation of very weak absorption transitions (forbidden transitions) and the study of harmonic transitions in the visible range [CAM 90].

The dynamics of a multimode laser (dye laser or Ti:sapphire) is described by a system of coupled balance equations between the population inversion of the amplifying medium and the photon density in each cavity mode (as, for example, in

Chapter 6, [DAH 16]), so that the temporal evolution, after gain saturation, of the averaged laser spectrum can be expressed by:

$$I(\sigma, t_g) \cong \frac{I_0}{\Delta\sigma}\sqrt{\frac{\Gamma t_g}{\pi}}\exp(-(\frac{\sigma - \sigma_0}{\Delta\sigma})^2 \Gamma t_g) \qquad [1.21]$$

where $\Gamma = 1/T$ is the inverse of the lifetime of a photon in the cavity, σ_0 is the center of the gain profile, $\Delta\sigma$ is the laser gain linewidth, and t_g is the laser generation or operation time.

The exponential function describes the temporal evolution of the Gaussian base line of the laser spectrum. Its amplitude increases as $\sqrt{t_g}$, and its width decreases in time as $1/\sqrt{t_g}$. As already described, by introducing a gas in the cavity, the modes of the laser in coincidence with a transition, grow at a slower rate than that of the neighboring modes, the absorption in this case being considered as selective losses [PAK 70, PET 71, BEL 72, KEL 72]. The lines appear in the laser spectrum and grow with laser generation time. The observed spectrum can be considered as a superposition of the laser spectrum and that of the absorption spectrum of the gas inserted in the cavity.

The intensity transmitted by the cavity $I_t(\sigma)$ [PER 96] can thus be calculated using equation [1.5], according to the Beer–Lambert law:

$$I_t(\sigma, t_g) \cong I(\sigma, t_g)\exp(-\alpha(\sigma) l_{eq}) \qquad [1.22]$$

where $I(\sigma)$ is the intensity of the intracavity laser radiation and l_{eq} is the thickness of the gas through which it travels, or the equivalent absorption length following multiple reflections in the cavity such that:

$$l_{eq} = \frac{l_{gas}}{l_{cavity}} c t_g \qquad [1.23]$$

where l_{gas} is the optical path of the beam in the gas, l_{cavity} is the optical length of the cavity, and c is the speed of light.

For a time of 100 μs, an occupancy rate of 33% leads to an equivalent length traveled in the gas of about 10 km.

The quantitative measurements require the control of the temporal evolution of the laser and the capability to record the laser spectrum at a given instant equal to t_g. When a laser is initiated by the optical noise generated by the spontaneous emission resulting from vacuum fluctuations, the process is stochastic and the spontaneously emitted photons are distributed over all of the longitudinal modes (it is admitted that a diaphragm placed in the waist can limit the modes transversal to TEM_{00}) of the cavity. The average of N spectra makes it possible to reduce the noise according to $\sqrt{N}$. Losses due to the scattering centers should be avoided, although they cannot always be eliminated despite the use of thick mirrors. One method involves the use of a ring laser, which also has the advantage of increasing the equivalent path length. Laser generation times that are too long should also be avoided, as the Beer–Lambert law is then no longer applicable. The absorption spectral width must remain below the gain spectral width of the laser. The laser setup also comprises a high resolution monochromator, coupled to an array of photodiodes for the detection of the light issued from the laser cavity. Two synchronized acousto-optical modulators can be used, on the one hand, to interrupt the laser operation, and, on the other hand, to inject the laser output in a spectrograph after a time interval t_g. A synthesis on laser intracavity absorption spectroscopy can be found in [BAE 99] and [RAH 05].

1.3.2. *Cavity ring-down spectroscopy (CRDS)*

While Fourier transform spectroscopy originated in the 1960s, CRDS or similar techniques date back to the end of the 1980s. As previously described, there is an earlier work [PAK 70], which shows that the structure of the line spectrum of a laser, with inhomogeneous broadening of the amplification line, was due to losses depending on the intracavity laser frequency. The first CRDS study is usually cited in reference to the work of O'Keefe and Deacon [OKE 88] because they describe this spectroscopic technique by using the term cavity ring-down (CRD). It relies on the measurement of the absorption rate, in opposition to the measurement of the absorption amplitude of a light pulse confined in a closed optical cavity, with a high quality factor Q.

In a patent, Lehmann proposed the use of CRDS with a continuous monomode laser involving a monomode excitation of the cavity and an improvement of sensitivity [LEH 96]. The first CW-CRDS (Continuous Wave-Cavity Ring-Down Spectroscopy) measurements were conducted by Romanini *et al.* [ROM 97a, ROM 97b]. Subsequently, various CRDS variants are then applied with continuous lasers, in order to optimize cavity injection, such as cavity-locked ring-down spectroscopy [PAL 98] and OF-CRDS (Optical-Feedback CRDS) [MOR 04b]. CRDS is applied to an extended spectral range (spanning from UV to IR) for various applications: the fundamental spectroscopic characterization of weak transitions [MEJ 08, PEA 96, ROM 93, ROM 95], trace detection [MEI 94, SCH 94] or the detection of radicals in flames [MEI 94]. A synthesis of CRDS can be found in [SCH 97].

A typical CRDS device in pulsed mode (Figure 1.13) is composed of a pulsed laser source (dye lasers in the visible range), a high finesse optical cavity (of length L) and a detection system. It is important to recall that the finesse increases with the reflective power of the cavity mirrors. If the duration of the laser pulse t_L is small compared to the back and forth time in the cavity ($t_{ar} = 2L/c = 10^{-20}$ ns for $L = 1.5\ 10^{-12}$ m), light does not interfere with itself in the cavity. A stable fraction of the laser pulse (of about 10^{-5}) is injected by transmission in the cavity by the input mirror. For a typical energy pulse of 1 mJ, this fraction corresponds to 3×10^{10} photons.

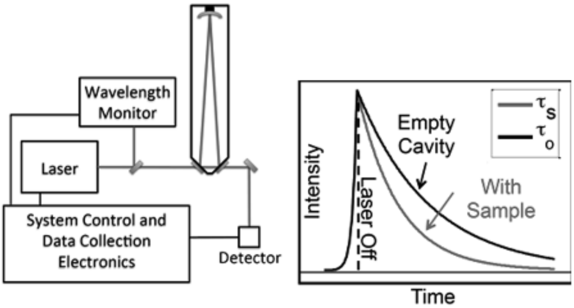

Figure 1.13. *Diagram of a CRDS setup and temporal profile of the optical signal in the absence and in the presence of an absorbent. For a color version of this figure, see www.iste.co.uk/dahoo/infrared2.zip*

The laser pulse trapped inside the cavity undergoes multiple reflections, and at each reflection, it loses a part of its energy, which is released after transmission on the mirror in front of the cavity. The temporal profile of the observed transmitted signal is then formed by a succession of pulses, whose intensity gradually decreases (Figures 1.13 and 1.14) $I(t) = I_0 \exp(-\tau/t)$, where the time constant τ depends on the presence or absence of an absorbent in the cavity.

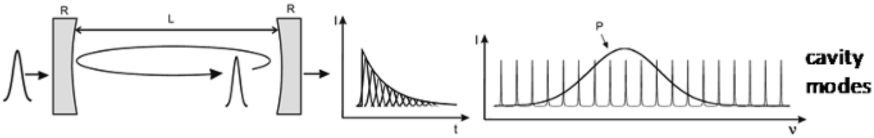

Figure 1.14. *Temporal profile of the transmission of a laser pulse and spectral profile P of the laser pulse on the cavity mode comb*

It is important to note that the laser pulse spectrum splits over several longitudinal resonance modes of the cavity ($\Delta\nu = c/2L$ and the transverse modes are not considered). Laser resolution (dye laser ≅ 0.07 cm^{-1}, Ti-sapphire ≅ 0.17 cm^{-1}, $\Delta\nu = c/2L = 0.0115\ \text{cm}^{-1}$ for $L = 43.5$ cm) must be higher than the gap between modes, so that the absorption lines appear in the laser gain profile.

Assuming that the Beer–Lambert law can be applied, the detected intensity is given by $I_t(\sigma) = I_0 \exp(-\sigma Cl)$, where $I_t(\sigma)$ is the intensity transmitted at the wave number σ, C is the concentration of the absorbent and l is the length of the sample traveled by the wave, following multiple back and forths of the beam in the cavity. The absorption coefficient α is defined by the product Cl so that the transmitted intensity can be written according to equation [1.22]: $I_t(\sigma, t_g) \cong I(\sigma, t_g)\exp(-\alpha(\sigma)l_{eq})$.

The calculation of the intensity after n passes in the cavity leads to the expression:

$$I_n = (Rexp(-\alpha L))^{2n} I_1 = I_1 \exp(-2n(-lnR + \alpha L)) \qquad [1.24]$$

which expresses the laser intensity detected by the photoconductor, after n back and forths in the cavity and where $I_1 = T^2 I_0 \exp(-\alpha L)$, with R being the reflection coefficient of the mirrors, T the transmission coefficient of the mirrors and I_0 the intensity of the laser injected in the cavity. With the reflection coefficient being close to unity, lnR is approximated by $-(1 - R)$. By putting $t = 2nL/c$ for the time duration of the path on n back and forths in the cavity, an expression depending on time t is obtained:

$$I(t) = I_1 \exp\left(-\frac{t}{\tau_S}\right) \qquad [1.25]$$

with:

$$\tau_S = \frac{L}{c\big((1-R)+\alpha L\big)} \qquad [1.26]$$

The CRDS decay time in the absence of an absorbent has the following expression:

$$\tau_0 = \frac{L}{c(1-R)} \qquad [1.27]$$

where L is the distance between the mirrors, c is the speed of light, and R is the reflectivity of the mirrors. τ_0 is obtained by putting $\alpha = 0$.

Equation [1.26] directly gives the absorption coefficient α in the form:

$$\alpha = \frac{1}{c\,\tau_S} - \frac{1-R}{L} = \frac{1}{c\,\tau_S} - \frac{1}{c\,\tau_0} \qquad [1.28]$$

The time τ_0 or τ_s, referred to as decay time or ring-down time, represents the average duration of the trapping of the light energy in the resonator. The measurement of this time is the fundamental principle of CRDS. The ring-down time is measured for a given number of waves and leads to the absorption coefficient. It is important to note that the effective length L_{eq} traveled by light is equal to $L_{eq} = c\tau$. For a cavity of length L =1 m and a reflectivity coefficient $R = 0.9998$, $\tau = 16.7$ µs. This corresponds to an effective length traveled $L_{eq} = c\tau = 5$ km. For low intensity signals, the formula [1.28] leads to $\delta\tau/\tau = \delta\alpha/\alpha$. The sensitivity of the technique leads to a detection limit imposed by the noise $\delta\tau_N$, which is $\delta\alpha_N = \delta\tau_N/(\tau L_{eq})$. For a molecule such as methane, CH_4, which presents isolated absorption lines, the latter appear on a nearly constant horizontal base line, depending on the wave number related to the term $(1-R)/L$. For triatomic molecules such as CO_2, which present a dense absorption spectrum, it is necessary to have an independent measurement of the base line obtained with an empty cavity, in order to measure the absorption coefficient of isolated lines.

The pulse injection in the optical cavity can be easily achieved with pulsed lasers. The technique is insensitive to the fluctuations in intensity of the laser pulse, which is one of the main noise sources with direct absorption measurement methods. For the dye lasers, these fluctuations are on average about 10%. The dye lasers (Figure 1.9) make it possible to cover a spectral range that extends from the IR to near ultraviolet by using doubling or mixer crystals. Given that the developed systems are robust and shielded from vibrations, the minimal detectable absorption coefficient ranges between 10^{-6} cm^{-1} and 10^{-10} cm^{-1}.

In pulsed CRDS, the width of the laser pulse spectrum and the poor quality of the spatial profile of the laser beam are drawbacks that led to the development of continuous wave CRDS (CW-CRDS). In practice, the spectrum of the laser pulse splits over several longitudinal modes (Figure 1.14) and over several higher-order transverse modes. The result is a profile gap with respect to the exponential function of the intracavity field ring-down. It is important to note that the spectral width of the laser pulse must be below that of the targeted space to be able to detect its absorption. These limitations of pulsed lasers are eliminated when a continuous emission mono-frequency laser is coupled to the resonance modes of the cavity.

CW-CRDS involves tuning a continuous emission monochromatic (mono-frequency) laser on a resonance mode of a high-finesse optical cavity. Compared to the pulsed CRDS, CW-CRDS is more difficult to implement, due to the need to effectively inject over a sufficient time duration, the narrow laser spectrum (of the order of MHz for a telecommunication laser diode, for example) in the narrower mode of the cavity modes ($\simeq$10 kHz). CW-CRDS was developed by Romanini *et al.* at the end of the 1990s, first with a dye laser [ROM 97a] and then with a laser source with an external cavity [ROM 97b], and in 2004 with a fiber telecommunication laser diode (of distributed feedback (DFB) type) [MOR 04].

The diagram of the setup used by Romanini *et al.* [ROM 97a] is illustrated in Figure 1.15. The cavity consisting of two mirrors of very high reflectivity is linear and the injection in the cavity is achieved by a simple passage through resonance, without frequency control. The cavity length is modulated by applying an electrical voltage on the piezoelectric plate (P) that supports one of the mirrors. The intensity transmitted by the cavity is focused on the photodiode. Thanks to modulation and continuous and single-frequency emission, scrolling of the $\mathrm{TEM}_{m,n}$ modes of the cavity can be displayed. This configuration can be used for precise optical alignment in order to reach a spatial agreement between the laser and a TEM_{00} mode of the cavity.

The signal emitted from the length-controlled cavity is directed towards a threshold detector circuit. When the state of the system is such that the fixed frequency of the laser coincides with that of the resonance, and the intracavity field reaches a threshold value, the circuit rapidly (≈ <1 μs) interrupts the acousto-optical modulator that deflects the beam towards the cavity entrance. The modulator plays the role of a switch and sends a significant fraction (80%) of the laser beam towards the cavity in position 2. A ring-down signal can be recorded with a high SNR, in theory, with a transmitted intensity equal to the incident intensity. At the end of the recording, the modulator sends the laser beam to its initial position waiting for a new injection in the cavity. The transmission signal of the cavity is digitized and digitally processed by software.

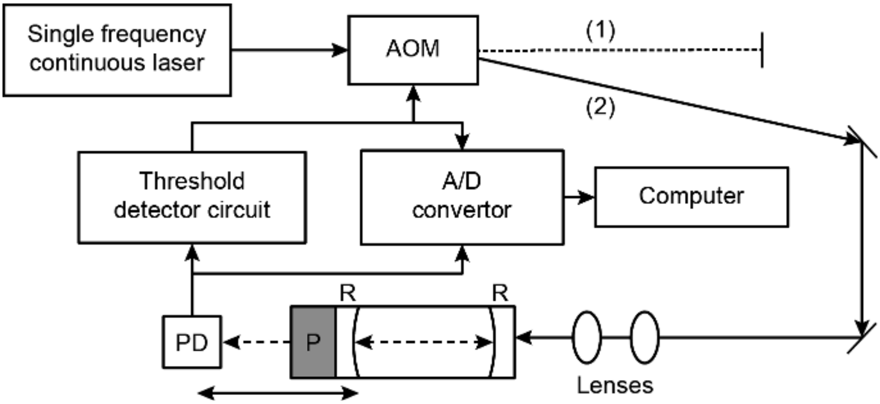

Figure 1.15. *CW-CRDS by injection through resonance [ROM 97a]: P, piezoelectric; AOM, acousto-optical modulator; PD, photodiode; A/D, analog-to-digital converter [DOM 97a, DOM 97b]*

The duration of the measurement can be less than one second for an average over 100 measured decay times. The measurement of the ring-down time is not affected by the amplitude noise from the conversion of the laser phase noise by the cavity, and which results from its greater width than that of the longitudinal mode of the cavity. CW-CRDS typically allows a detection dynamic covering 3 to 4 orders of magnitude (varying from 10^{-5} cm^{-1} to 10^{-9} cm^{-1}).

The repetition rate of the ring-down time is limited by the modulation frequency of the cavity (>100 Hz) in CW-CRDS, while in pulsed CRDS it depends on the laser used (often ≃10 Hz only). Reproducibility of the ring-down time values, from one measurement to another, is of about 0.1% in CW-CRDS and of about 1% with systems employing pulsed CRDS. This difference is directly linked to the stability of the laser source. With CW-CRDS, the laser is spectrally and spatially stable, while a pulsed laser presents spectral distribution fluctuations and spatial fluctuations. Therefore, from one measurement to another, the excited transverse and longitudinal modes are not the same, which leads to different ring-down time values.

Since the spectral width is generally determined by the laser width, CW-CRDS provides a gain in spectral resolution compared to pulsed CRDS. In the first case, it is of the order of MHz (for a DFB diode) and in the second case, it is of the order of GHz. Hence, it is suitable for atmospheric trace-gas detection. Moreover, the use of laser diodes in CW-CRDS allows for a significant reduction in the size of the optical system and its cost. A disadvantage of CW-CRDS is the limited availability of laser sources, in particular of laser diodes in certain spectral regions, which moreover only provide a limited scanning range.

1.3.3. *Frequency comb spectroscopy (FCS)*

At the end of the 1990s, the mode-locking technique led to a breakthrough in the precision of frequency and time measurements thanks to laser frequency combs [HÄN 06, HAL 06]. The steady pulse train of a mode-locked femtosecond laser can give rise to a steady comb spectrum composed of 1 million modes with equal spacing at the pulse repetition frequency. The frequency of the electromagnetic waves in this optical range varies between $4,010^{14}$ Hz and $7,510^{14}$ Hz. The measurements of absolute phase coherence of these frequencies proved difficult [CUN 01]. Electronic techniques can be used to measure and directly generate radiofrequencies (RF) up to several hundred GHz. Nowadays, the most stable and precise frequency standards are achieved in the RF range on the basis of hyperfine transitions of cesium at 9.2 GHz and of hydrogen at 1.42 GHz. The transition of cesium is used to define the second in the international system of units (SI).

The development of studies related to mode-locking dates back to the beginning of the 1960s [DID 64, HAR 64, YAV 65] with the description of the generation of a continuous train of pulses by the modulation of the internal losses of a He–Ne laser cavity by means of an acousto-optical modulator. Mode-locking involves phase synchronization of the longitudinal modes of a laser, therefore reaching an in-phase state. If at a given instant t, the electrical field of each mode is at a maximum, the laser output is a pulse centered on the value t. The greater the number of synchronized modes, the shorter the duration of this pulse. There are a variety of locking techniques, the most commonly used being dye lasers with saturable absorption, the use of an acousto-optical modulator or the Pockels cell. The temporal width of the pulse depends on the width of the gain envelope, since the number of longitudinal modes on which the laser can operate depends on the losses of the cavity (Figure 1.12). From 1960 to 1970, the mode-locking technique was implemented on various types of lasers: gas lasers [DEM 65, DEC 68, WOO 68], solid lasers [DEU 65, DEM 66, DID 66], liquid dye lasers [GLEN 68, BRA 68, SAM 68, SCH 68] and semi-conductor lasers [MOR 68].

In a multimode laser, there is *a priori* no phase relation between the longitudinal modes oscillating in the cavity, since their phases are not fixed and randomly vary, mainly due to the action of spontaneous emission. Consequently, interference between longitudinal modes are not constructive, and the power fluctuations they generate are on average zero, leading to the emission of constant optical power. If the modes are interconnected by a fixed phase relation, they can constructively interfere. The beats then produce a modulation of the intracavity optical power, potentially leading to the generation of pulses (Figure 1.16), whose period corresponds to the time it takes light to go back and forth in the cavity. In this case, the laser is known as mode-locked laser.

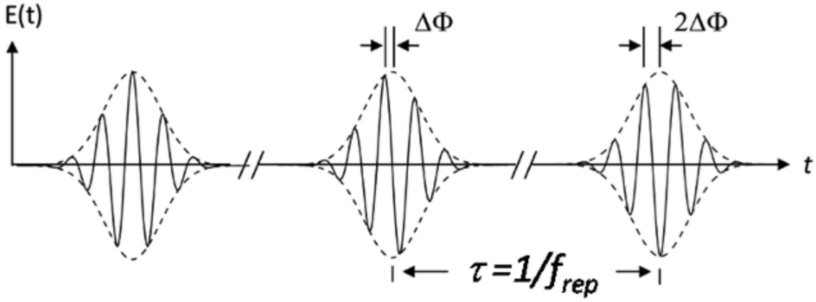

Figure 1.16. *Pulse train emitted by a laser source in the temporal range*

In the frequency range (Fourier transform), the intensity spectrum of a pulse train is a frequency comb (Figure 1.17). The phase difference $\Delta\Phi$ between the envelope and the pulse carrier leads to an offset f_0 in the frequency spectrum. Each peak is separated by the repetition frequency f_{rep} of the pulses. The line frequency f_n is given by the relation $f_n = nf_{rep} + f_0$. It is essential to properly control the values of parameters f_{rep} and f_0. In this case, the device behaves like a set of single-frequency lasers, or thousands of lasers that can be used as an optical rule. In practice, mode locking in a laser cavity is classified into two categories: active and passive.

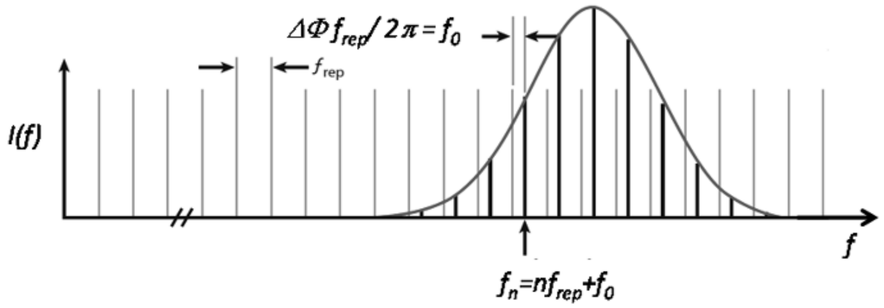

Figure 1.17. *Pulse train emitted by a laser source providing a frequency comb in the time domain. For a color version of this figure, see www.iste.co.uk/dahoo/infrared2.zip*

Active mode locking can be done by an external signal that generates a modulation of the intracavity field. The external modulated signal can be electrical, by modulation of the current injected into the device, or optical, by non-resonant injection into the cavity of a modulated optical signal. This amplitude modulation generates sidebands that are superimposed onto the cavity modes when the modulation frequency is identical to the spectral interval between modes. The fixed phase relation between these modulation sidebands is then transferred to the cavity modes, leading to their phase locking. The active mode locking with loss modulation can be achieved with acousto-optical modulation with an external RF signal. An acousto-optical modulator for mode locking differs from that used for Q-switching: an acousto-optical mode locker is a continuously operating Bragg diffraction unit with stationary wave, while an acousto-optical Q-switch is a Bragg diffraction unit that is switched on and off in order to switch the Q cavity between two different values. Synchronous pumping can also be used to generate ultra-short pulses, considered to be active mode locking by gain modulation. The gain medium is periodically pumped, either optically or electrically, with a train of very short pulses at the same repetition rate as that of the periodic arrival in the gain medium of the pulse circulating inside the laser cavity.

Passive mode locking can be achieved by using a storable absorber located near an edge of a linear cavity. Sometimes, a saturable absorber used for the passive

Q-switch can also be used for passive mode locking, but the requirements for passive mode locking are very different from those for passive Q-switching. Passive mode-locking techniques rely on the intrinsic properties of the elements of the laser cavity to generate self-modulation of the optical power, i.e. without using an external signal. The phase synchronization of modes can be achieved by using a saturable absorber inside the laser cavity [NEW 74, HAU 75], the optical Kerr effect [NEG 91, SPE 91, ASA 93] or nonlinear gain effects [STA 67, NOM 02]. For example, passive mode locking with a saturable absorber can be achieved in a ring configuration. In this configuration, two intracavity laser pulses travel through the saturable absorber in opposite directions, rapidly decreasing the gain at the profile center (Lamb dip).

With a Ti:sapphire laser, which has a broadband gain profile, it is possible to obtain pulses of the order of the femtosecond, typically of 5 fs, since the number of locked modes can be high. Hence, mode locking makes it possible to obtain very short duration optical pulses of the order of the femtosecond. The development of mode-locked lasers and their applications to metrology was thus made possible thanks to the development of femtosecond sapphire titan lasers (Ti^{3+}:Al_2O_3). Moreover, combined with the width of their gain band, the mode locking phenomenon induced by the Kerr effect in this type of laser allows the formation of an optical frequency comb. The very strong phase coherence between the modes of the laser cavity, forming a comb whose spectral interval is constant, is adapted to the precise measurement of optical frequencies. This led to the joint award of the Nobel Prize for Physics in 2005 to J. L. Hall and T. W. Hänsch. Since its discovery, the optical frequency comb has revolutionized the field of metrology. More specifically, it provides spectroscopy with a multipurpose tool for the synthesis and measurement of optical frequencies with extremely low relative uncertainties, from 10^{13} to 10^{15}. The evolution of the frequency comb technique is described in a number of publications, among which are the following: [STO 08], [YE 10], [DID 10], [PIC 19].

The extension of frequency combs based on mode locking lasers in the MIR range is not easy [SCH 12]. Though it is possible to develop an average IR comb by using a nonlinear frequency conversion from a near-IR frequency comb [MAD 06, DEL 07, MAL 08, ADL 09, GUB 09, WON 10, LEI 11, KEI 12, ULV 14, PAP 14], these technologies are still quite complex. Consequently, MIR high-precision spectroscopy is often conducted by referencing the MIR laser source to a NIR optical frequency comb, via a nonlinear frequency conversion. In this IR range, recent works are described in [MEN 20, GAT 20, LIN 20b, DID 20].

The authors of [GAT 20] describe the development of a high power mid-IR frequency comb with a repetition frequency of 100 MHz and a pulse duration of 100 fs. The frequency difference is generated between two branches derived from an Er:fiber comb, amplified separately in Yb:fiber and Er:fiber amplifiers. Average powers of 6.7 W and 14.9 W are, respectively, generated in the forwarding signal of 2.9 µm and 1.6 µm. With a high average power, an excellent quality of the beam and a passive phase stabilization of the carrier envelope, this light source is a platform that allows the generation of broadband frequency combs in far IR, visible and far ultraviolet.

In [LIN 20b], IR frequency combs are developed for the atmospheric window in mid-IR from 3 to 5.5 µm and contain valuable information concerning the molecular composition and the function that is significant in the atmospheric processes for fundamental and applied spectroscopy. Using a fiber laser source with robust mode locking, of pulse < 11 fs in the near IR, the quadratic nonlinear optical processes ($\chi(2)$) were investigated, which led to the generation of frequency combs over any atmospheric window in mid-IR. Experiments and modeling proved the generation of intra-pulse difference-frequency that produces average IR pulses of several cycles in a single passage through lithium niobate of periodic polarization. Moreover, the harmonic and cascade $\chi(2)$ nonlinearities provide direct access to the carrier envelope offset frequency of the driving pulse train in the near IR. The high-frequency stability of the mid-IR frequency comb is used for the spectroscopy of acetone and for carbonyl sulfide with simultaneous bandwidths above 11 THz and with a spectral resolution of 0.003 cm^{-1}. The combination of a low noise and wide spectral coverage allows the detection of gas traces of concentrations of about one part per billion.

The rise of frequency combs pushes the frontiers of very high resolution molecular spectroscopy into the spectral range of mid-IR. The works of Chen, Hänsch and Picqué [CHE 19] show that a multiplexed metrology of line shapes is expected by Fourier transform spectroscopy in the mid-IR using two frequency combs. This method can be used to limit the effect of measurement distortion on the line shape, a high SNR and the possibility of having access to a broad spectral bandwidth for the high-precision spectroscopy of small molecules.

[FOR 19] and [DID 20] describe the development and improvement of optical combs throughout the last 20 years. Optical clocks, based on optical transitions of atoms, operate at a much higher frequency than microwave atomic clocks currently used as synchronization norms. Better stability is reached with the prospect of being able to redefine the second. Development of stable and self-referenced optical frequency combs that span from microwaves to optical wavelengths was the key to research efforts. Many applications go from precision synchronization to spectroscopy, high resolution imaging, range finding and navigation or space exploration.

1.4. Spectroscopy for space observation

This section describes two other examples of devices used for space observation and analysis, one *ex situ* and the other aboard a space probe. Ellipsometry was used to determine the optical constants of tholins, aerosols present in the atmosphere of planets, namely the Titan satellite, which orbits Saturn. A spectrometer (SOIR) based on an AOTF was used to collect data on the molecules present in the atmosphere of Venus.

1.4.1. *Spectroscopic ellipsometry for space observation*

Ellipsometry is a non-destructive optical technique that can be used for the study of materials in the form of thin layers. The technique is sensitive to surfaces and interfaces. Samples can be prepared by deposition on a substrate and then a spectroscopic ellipsometer, in the near IR–mid-IR range or in the visible range, can be used to determine the optical refractive indices. Studies on tholins present in the atmosphere of Titan were conducted in this context. This technique is widely described in the literature [AZZ 77, DRE 82, BOC 93, PIC 95, VED 98, TOM 99, OHL 00, TOM 2005, FUJ 07].

A synthesis of this technique, as well as the inverse method required for the analysis of ellipsometric data, can also be found in [DAH 19b] and [DAH 16]. Ellipsometry involves the study of the polarization state of light after reflection on the surface of a sample in order to determine its physical and optical characteristics, particularly its refraction index, and also its thickness and rugosity. The reflected electric field E_r can generally be decomposed into two components of orthogonal polarizations, E_{rp} and E_{rs}, whose amplitudes determine the ellipticity of the reflected wave. This ellipticity is characterized by the ratio:

$$\frac{E_{rp}}{E_{rs}} = \frac{r_p Ei_p}{r_s Ei_s} = \rho \frac{E_{ip}}{E_{is}} \quad \text{with } \rho = \frac{r_p}{r_s} = (\tan\psi) e^{i\Delta} \qquad [1.29]$$

where E_{ip} and E_{is} correspond to the amplitudes of the electric field of the incident wave. The reflection coefficients r_s and r_p in amplitude of waves *p* (parallel to the incidence plane) and *s* (perpendicular to the incidence plane) are expressed in terms of complex indices $\tilde{n}_i = n_i + ik_i$ (n_i is a real index characterizing the polarization of matter by the electric field of the wave and k_i is an imaginary index characterizing the absorption of light energy by matter, Chapter 5, equations [5.11] and [5.12], [DAH 16]) and the reflection and refraction angles (Fresnel formulas, equations [1.33] and [1.34]) of the two media on both sides of the surface or diopter).

Based on the initial polarization state of the incident wave E_i and the measurement of the polarization state after reflection, an ellipsometer provides the ellipsometric parameter ρ (equation [1.29]) that can be expressed as a function of two other ellipsometric parameters Ψ and Δ, which are related to variations of the ellipse shape (ratio of minor and major axes, orientation) and can be used to determine ρ. Irrespective of the technique employed, the instrumentation comprises the optical instruments shown in Figure 1.18, two inclinable arms and a sample support. One of the arms is composed of a source of light and an optical setup yielding an incident wave of known polarization. The other arm is made up of an analyzer and a detector for the measurement of the polarization state of the wave reflected by the sample.

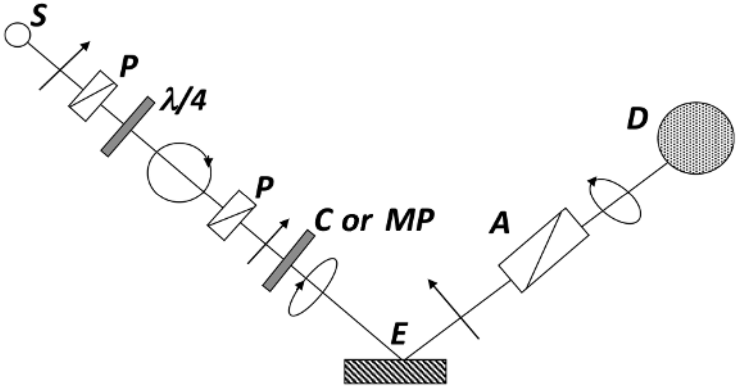

Figure 1.18. *Elements of an ellipsometer: S, source; P, polarizer; λ/4, quarter wave plate; C, compensator; MP, phase modulator; E, sample; A, analyzer; D, detector [DAH 16]*

The measurement and analysis process comprises the following stages:

– preparation of the initial state of polarization of the incident light;

– light–matter (sample) interaction and reflection;

– measurement of the polarization state of the reflected wave;

– calculation of the ellipsometric parameters Ψ and Δ or $tan(\Psi)$ and $cos(\Delta)$);

– evaluation of random and systematic errors on Ψ and Δ;

– determination of the physical properties of the material (n_i, k_i, e_i, etc.), complex indices and thicknesses from Ψ and Δ using a numerical optimization method (inverse problem).

The analysis of ellipsometry data is an inverse problem of deterministic optimization, such as that described in Chapter 2 of [DAH 16]. The optimization is conducted by comparing the experimental values to the theoretical ellipsometric parameters calculated from a model [AZZ 77, DRE 82, BOC 93, PIC 95, VED 98, TOM 99, OHL 00, TOM 2005, FUJ 07, DAH 04a, DAH 04b, FRA 05, NOU 07, LOU 07, LOU 08, DAH 10, SCI 10, MAH 11, CAR 12, SCI 12, MAH 14].

The ellipsometric parameters Ψ and Δ or ($tan(\Psi)$ and $cos(\Delta)$) measured by the ellipsometer are stored for each wavelength λ in digital form in a file. Each wavelength is identified after scattering through a grating on a diode array or a set of photomultiplier tubes. The data are stored in discrete form for each wavelength detected.

The analysis involves the comparison, for each wavelength, of the values of parameters ψ_{th} or $tan(\psi_{th})$ and Δ_{th} or $cos(\Delta t_h)$ calculated from structural models (multilayers) and optical models (dielectric function or complex index) to the measured values of ψ_{exp} or $tan(\psi_{exp})$ and of Δ_{exp} or $cos(\Delta_{exp})$. The structural model corresponds to the type of multilayer considered for the structure of the studied layer. For example, for a system composed of air, layer, substrate, there are three media to be considered for each wavelength. When the surface rugosity is taken into account, the multilayer comprises an additional layer (Figure 1.18).

In order to calculate the various reflection and transmission coefficients at the interface of various layers forming the structure of a sample, the matrix methods of Abeles [ABE 50] or of Hayfield and White [HAY 64] can be applied.

Considering the multilayers in Figure 1.18, the axis Oz being oriented downwards, the thickness of layer i is denoted by e_i and its complex index by $\tilde{n}_i=n_i+k_i$, where n_i and k_i are the real and imaginary parts of the complex index, respectively. θ_i is the angle of incidence of the incident ray in layer i. These parameters can be used to calculate the global Fresnel coefficients for a sample by means of the Abeles matrix formalism [ABE 50] and then deduce by inversion the ellipsometric parameters of the sample.

At the coordinate z, the total electric field is the sum of two components, one that propagates towards ascending z (hence towards the substrate) and the other towards descending z (towards the surface of the sample) denoted, respectively, by $E^{+}(z)$ and $E^{-}(z)$. The beam is linearly polarized either p or s, and this property is preserved across the layers. The field at two depths z and z' is connected by the matrix transformation:

$$\begin{pmatrix} E^+(z') \\ E^-(z') \end{pmatrix} = \begin{pmatrix} S_{11} & S_{12} \\ S_{21} & S_{22} \end{pmatrix} \begin{pmatrix} E^+(z) \\ E^-(z) \end{pmatrix} \qquad [1.30]$$

Assuming that z and z' are the coordinates on both sides of the interface $i/(i+1)$, the expression of the interface crossing matrix $I_{i,i+1}$ is:

$$I_{i,i+1} = \frac{1}{t_{i,i+1}} \begin{pmatrix} 1 & r_{i,i+1} \\ r_{i,i+1} & 1 \end{pmatrix} \qquad [1.31]$$

where r and t are Fresnel coefficients.

Depending on the type of polarization p or s, these coefficients are expressed as:

$$r_{pi,i+1} = \frac{n_{i+1}\cos\theta_i - n_i\cos\theta_{i+1}}{n_{i+1}\cos\theta_i + n_i\cos\theta_{i+1}} \qquad r_{si,i+1} = \frac{n_i\cos\theta_i - n_{i+1}\cos\theta_{i+1}}{n_i\cos\theta_i + n_{i+1}\cos\theta_{i+1}} \qquad [1.32]$$

and:

$$t_{pi,i+1} = \frac{2n_i\cos\theta_i}{n_{i+1}\cos\theta_i + n_i\cos\theta_{i+1}} \qquad t_{si,i+1} = \frac{2n_i\cos\theta_i}{n_i\cos\theta_i + n_{i+1}\cos\theta_{i+1}} \qquad [1.33]$$

Two matrices $I_{i,i+1}$ are calculated, one for each type of polarization.

Relating z and z' to the layer i, of thickness e_i, the propagation matrix in the layer is expressed as:

$$\mathrm{T}_i = \begin{pmatrix} e^{i\delta_i} & 0 \\ 0 & e^{-i\delta_i} \end{pmatrix} \qquad [1.34]$$

where $\delta_i = \frac{2\pi}{\lambda} e_i n_i \cos(\theta_i)$

The expressions of matrices T correspond to an isotropic layer and do not depend on polarization. The response corresponding to the stacking of N layers crossed by the beam is obtained after multiplication of the matrices by placing z' at the level of the substrate and z at the level of the ambient medium. The successive angles in each layer are related by the Snell–Descartes law. The expression of the matrix corresponding to a layer defined by N multilayers is given by:

$$S = I_{0,1}T_1 I_{1,2}T_2 \ldots I_{i,i+1}T_{i+1} \ldots T_{N-1}I_{N-1,N} = \prod_{i=0}^{N-1}\left(I_{i,i+1}T_i\right) \qquad [1.35]$$

The matrix product for each polarization leads to the expressions of global Fresnel coefficients in the following form:

$$r_p = \frac{S_{21p}}{S_{11p}} \text{ and } r_s = \frac{S_{21s}}{S_{11s}} \qquad [1.36]$$

This leads to:

$$\rho = \frac{r_P}{r_S} = \frac{S_{21p}S_{11s}}{S_{11p}S_{21s}} = (\tan\psi)\, e^{i\Delta} \qquad [1.37]$$

For example, for an air, layer, substrate system, for each wavelength λ_i, ψ and Δ are functions of five parameters, three indices that lead to three real parts and two imaginary parts and a thickness such that:

$$\Psi = f(n_a, n_s, k_s, n_f, k_f, e_f) \qquad [1.38]$$

and:

$$\Delta = g(n_a, n_s, k_s, n_f, k_f, e_f) \qquad [1.39]$$

where indices *a*, *s* and *f* correspond, respectively, to the ambient medium, the substrate and the film.

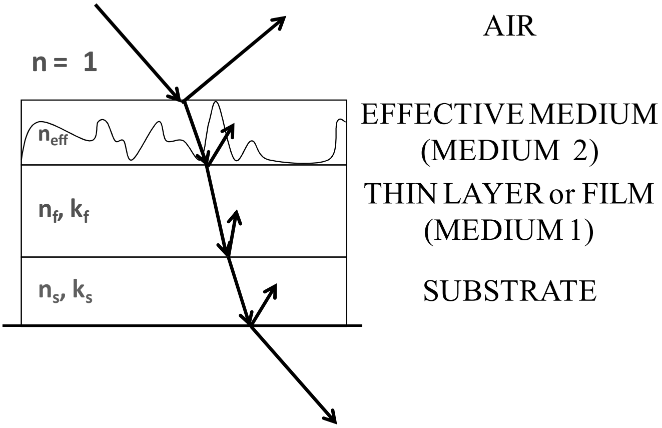

Figure 1.19. *Rough surface modeled by an effective medium. For a color version of this figure, see www.iste.co.uk/dahoo/infrared2.zip*

A cost or objective function (see Chapter 2, section 2.4.1 [DAH 16], [AZZ 77]) is defined based on ellipsometric parameters ρ_{th} and ρ_{exp}, in order to implement the minimization process. An example of cost function σ or MSE (*Mean Square Error*) that is used to estimate the gap between the calculated values and the measured values for a given angle of incidence can be expressed as follows:

$$\sigma = \frac{1}{n-m-1}\sum_{j=1}^{n}\frac{\left|\rho_{exp}(\lambda_j) - \rho_{th}(\lambda_j,\ X_j)\right|^2}{\left|\partial\rho_{exp}(\lambda_j)\right|^2} \qquad [1.40]$$

where n represents the number of experimental points, m is the number of relations between the equations (n-m-1 is the number of independent parameters, the air index is assumed to be known and equal to 1). In this expression, the denominator takes into account the SNR that is different on the measurement spectral range, which allows better adjustment of experimental data.

Depending on the ellipsometric angles, the following expression is used:

$$\sigma = \frac{1}{n-m-1}\sum_{j=1}^{n}\left(\frac{\left|\Psi_{exp}(\lambda_j) - \Psi_{th}(\lambda_j, X_j)\right|^2}{\left|\partial\Psi_{exp}(\lambda_j)\right|^2} + \frac{\left|\Delta_{exp}(\lambda_j) - \Delta_{th}(\lambda_j, X_j)\right|^2}{\left|\partial\Delta_{exp}(\lambda_j)\right|^2}\right) \qquad [1.41]$$

where $\partial\Psi$ or $\partial\Delta$ are the standard deviations of experimental data.

Two values, one for ψ and one for Δ, are measured per wavelength. The contribution of noise-contaminated measurements to the adjustment is minimized by the weighting of data by the inverse of standard deviations. In this expression, $X_j = (x_1, x_2, \ldots x_k)$ is a vector whose components are the various parameters to be adjusted. For example, in the case of a transparent isotropic film on an absorbent substrate, $X_j = (x_1 = n_f, x_2 = e_f, x_3 = n_s, x_4 = k_s)$ and therefore $k = 4$, the indices f and s corresponding to the film and substrate, respectively.

In the case of an absorbent film on a substrate, if the ambient medium is air ($n_{air} = 1$) of known index, there are only five unknowns to be determined ($k = 5$) with $X_j = (x_1 = n_f, x_2 = k_f, x_3 = e_f, x_4 = n_s, x_5 = k_s)$. There is interdependency between certain parameters of X_j, which complicates analysis and optimization. For example, there is a strong correlation between the optical index and the thickness, and in order to reduce the effect of this coupling, a certain number of measures should be implemented, depending on the number of parameters to be adjusted. It is possible to combine the data for several angles of incidence, for example. For three parameters to be adjusted (e_f, n_f and k_f), six series of measurements are required, therefore three angles of incidence (each time Ψ and Δ are measured).

A model of a more complex layer can be used to take into account the presence of roughness at the surface of a thin layer or at the interface between two layers. In this case, the film is decomposed into two other homogeneous layers, consisting of a medium of different indices, with plane surfaces (Figure 1.19). The first layer (medium 1) is composed of a material of unknown index and thickness. Above it, a second layer consists of an effective medium, corresponding to an air–material mixture, with an effective index and a certain amount of air inclusion for modeling the presence of rugosity (medium 2).

Two models are used (Figure 1.20): the Maxwell–Garnett (MG) model, which corresponds to inclusions (proportion $p_m << 1$) in a host matrix, and the Bruggeman (BR) model, which is applied when various materials are present in similar proportions.

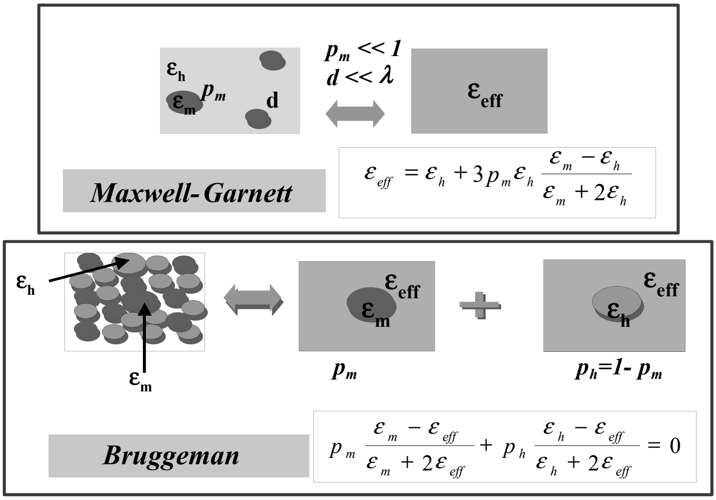

Figure 1.20. *Maxwell–Garnett and Bruggeman mean-field models. For a color version of this figure, see www.iste.co.uk/dahoo/infrared2.zip*

The following formula is used:

$$\frac{n_e^2 - n_h^2}{n_e^2 + 2n_h^2} = \sum_i f_i \frac{n_i^2 - n_h^2}{n_i^2 + 2n_h^2} \qquad [1.42]$$

where n_i is the index of inclusion, n_h is the index of the host medium, n_e is the index of the effective medium, and f_i is the inclusion fraction for the calculations of indices. The indices are related to the electric permittivity by the well-known relation $n_i = \sqrt{\varepsilon_i}$. The MG model considers that one of the two materials is the host material, i.e. $n_h = n_1$

or n_2 if two materials are present in the medium. The BR model considers the effective medium to be the host medium, and the index of the host material is replaced by $n_h = n_e$. For example, with the MG model, a certain thickness whose order of magnitude is close to the physical situation must be fixed, i.e. the thickness of the average roughness, as well as a fraction of the inclusion of air in the layer.

All of these parameters must also be adjusted by the fitting algorithm in order to minimize the gaps between the calculated and experimental values. Optimization is the search for the maximal or minimal value of a function $f(x)$ (Chapter 2, section 2.2, [DAH 16]) that can present local minima or maxima (Figure 1.21). This can always be dealt with as a minimization problem (in this case $-f(x)$) is optimized and the algorithm used must be able to reach the minimal value while avoiding local minima.

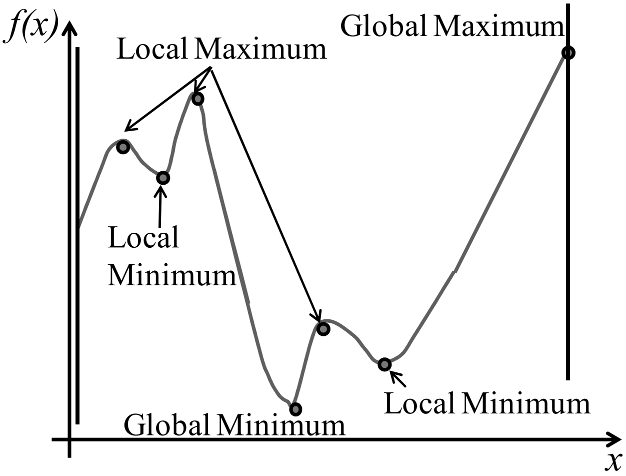

Figure 1.21. *Maxima and minima of a function. For a color version of this figure, see www.iste.co.uk/dahoo/infrared2.zip*

Generally speaking, since the models depend nonlinearly on the variables to be adjusted, the cost function σ is a nonlinear function of the parameters of $X_j = (x_1, x_2, \ldots x_k)$. The minimum can only be obtained by an iterative method: an initial estimation of parameters is refined at each stage until the parameters no longer vary. Inversion algorithms are generally used and they can be classified into two categories: those that require the calculation of gradient, such as gradient descent or conjugate gradient, of Newton, Levenberg–Marquardt (LM) [LEV 44, MAR 63], Davidon–Fletcher–Powell (DFP) [DAV 59, FLE 63] or Broyden–Fletcher–Goldfarb–Shanno (BFGS) [BRO 69, FLE 70, GOL 70, SHA 70]; and those that minimize the function without calculating the gradient, such as the Simplex method

[DAN 90] or closed methods [POW 64, BRE 73]. The commonly used algorithms in ellipsometry are the nonlinear simplex method of Nelder and Mead [NEL 65, PRE 86, pp. 521–528], a zeroth-order method that does not require the calculation of gradient, and of the LM and the BFGS methods, second-order methods that require the calculation of a gradient of the cost function for the evaluation of second-order derivatives. Second-order methods approach the cost function by an expansion limited to the second order.

The ellipsometry technique can be used to determine the optical constants of aerosols present in the atmospheres of planets or satellites of planets. This section presents the studies conducted on tholins, aerosols present in the atmosphere of Titan, satellite of Saturn [SCI 10, CAR 12, MAH 11, SCI 12, MAH 12a, MAH 12b, MAH 12c, MAH 14]. Sunlight scattering and absorption by the aerosols are an integral part of understanding the radiative balance of the planetary atmosphere covered by mist such as Titan's, and possibly the Earth's, early atmosphere. A key optical parameter of an aerosol is its refractive index.

Titan, the largest moon of Saturn, is surrounded by a very dense atmosphere. Since the beginning of the exploration of giant planets in the 1980s, Titan has focused a lot of attention on its unique atmosphere, characterized by thick mist. Based on radial intensity scans performed by the Voyager 2 space probe at high phase angles, Rages and Pollack [RAG 80] were able to determine the vertical distribution of scattered particles and to reveal a significant reduction in the density of aerosol particles under this layer.

Testing the numerical models used for the analysis of Titan observation data (albedo, radiative transfer, vertical profile of the mist, surface contribution, etc.) requires precise knowledge of the optical constants of Titan aerosol analogues or tholins. On Titan, the dissociation of N_2 and CH_4 by solar UV radiation and the electron bombardment of the Saturn magnetosphere induce a complex organic chemistry that leads to the production of solid aerosols in the stratosphere and upper atmosphere. These aerosols explain the orange mist that gives Titan its characteristic color. There is strong astrobiological interest in Titan's aerosols as they play an important role in the climate, composition and properties of Titan's atmosphere and surface.

In [SCI 10] and [SCI 12], the ellipsometry technique is used to determine the optical constants of the tholins produced by an RF plasma discharge in a gas mixture (95% N_2–5% CH_4) simulating the main atmospheric composition of Titan and deposited as a film on an Al–SiO_2 substrate (Figure 1.22).

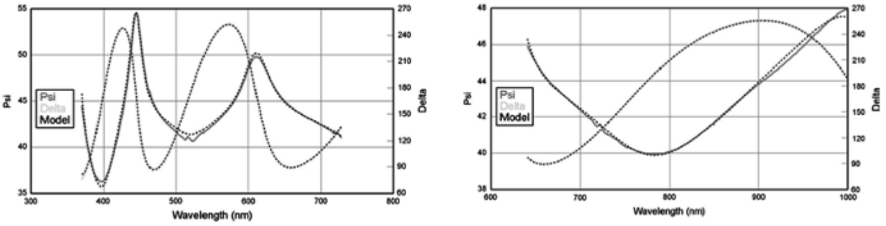

Figure 1.22. *Ellipsometric parameters ψ (Psi) and Δ (Delta) on the spectral range of 370–730 nm and 640–1,000 nm and adjustment in the dotted line. For a color version of this figure, see www.iste.co.uk/dahoo/infrared2.zip*

The real and imaginary parts, n and k, of the complex refractive index of tholins are determined over the spectral range from 370 nm to 900 nm by spectroscopic ellipsometry. The angle of incidence is fixed at 70°, close to Brewster's angle of SiO_2 substrate deposited on Ag or Au, and whose optical characteristics are preliminarily determined using Sellmeier's formula (equation [1.44]] adapted for transparent substrates. The optical constants of tholins are compared to those determined by other authors, and to the constants of Titan's aerosols, extracted from observation data provided by space probes (Figure 1.22), and are determined by Cauchy formulas for the real part and an exponential form for the imaginary part (equations [1.45] and [1.46]). Surface rugosity is modeled by the MG model

$$(n(\lambda))^2 = 1 + \sum_j {A_j\lambda^2}\Big/{\lambda^2 - \lambda_j^2} \qquad [1.43]$$

$$n(\lambda) = A + {}^{B}\!/_{\lambda^2} + {}^{C}\!/_{\lambda^4} \qquad [1.44]$$

$$k(\lambda) = \alpha e^{\beta hc\left({}^{1}\!/_{\lambda} - {}^{1}\!/_{\gamma}\right)} \qquad [1.45]$$

In formula [1.44], λ_j is the wavelength of the resonant absorption j and A_j is its absorption line force. In formulas 1.45 and 1.46, given n and k, A, B, C, α and β are adjustable parameters, γ is the limit of the forbidden band fixed at 250 nm for the adjustments, λ is the wavelength, h is Planck's constant, and c is the speed of light. The parameter A is connected to the approximate value of the amplitude of the refractive index of the material, and B and C are the parameters that give the profile of the index variation depending on the wavelength. The parameters α and β determine the profile of the extinction coefficient k. In the exponential formula (Urbach tail model) used for modeling the imaginary part of index k, the parameter γ is related to the forbidden band of the material, which can vary depending on its structure and composition.

In Figure 1.23, the real part of the refractive index, *n*, decreases from *n* = 1.64 (at 370 nm) to *n* = 1.57 (at 900 nm). The values *n* that are given are in agreement with those of tholins resulting from photochemistry [TRA 03] or discharge plasma DC [RAM 02]. The order of magnitude of *n* does not seem to depend on the production process of tholins. The values of *k* show two types of variations: an exponential decrease from 370 nm to 500 nm, with $k = 12.4\ e^{-0.018\lambda}$ (where λ is expressed in nm), followed by a plateau, with $k = (1.8 \pm 0.2)10^{-3}$.

This characteristic of a decreasing variation in two regimes is also observed in other studies of tholins though the change of slope does not always occur at the same wavelength. This may be related to the forbidden band in the absorption region and which depends on the structure of the material.

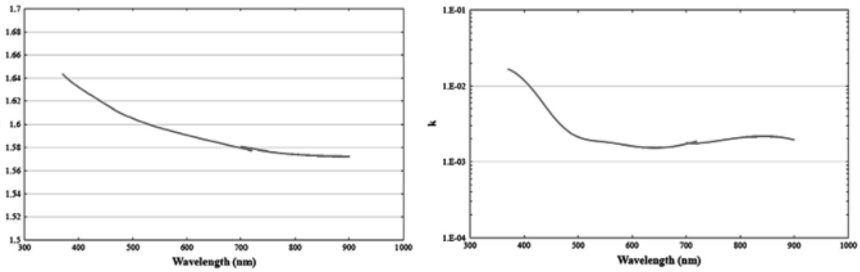

Figure 1.23. *Optical constants n and k in the 370–900 nm range. For a color version of this figure, see www.iste.co.uk/dahoo/infrared2.zip*

[MAH 12a], [MAH 12b] and [CAR 12] present the results of a study on the effect of various initial concentrations of methane during the preparation of tholin aerosols on the optical constants of tholins. Spectroscopic ellipsometry is used in the 370–1,000 nm range of wavelengths. As the thin layers of tholins are amorphous, the Tauc–Lorentz model (equation [1.47]) is used for the optical characterization

$$\begin{gathered} \varepsilon_2 = AE_0C\left(E - E_g\right)^2 / E\left(\left(E^2 - E_0^2\right)^2 + C^2E^2\right) \quad E > E_g \\ \varepsilon_2 = 0 \quad E < E_g \end{gathered} \qquad [1.46]$$

The expression of ε_2, the imaginary part of dielectric permittivity, comprises four energy parameters: the forbidden band, for example, the peak of joint density of states E_0, the broadening parameter *C* and the prefactor *A*, which includes the elements of the optical transition matrix [JEL 96]. The real part of the dielectric permittivity is then calculated using Kramers–Kronig relations (Chapter 5, equations [5.13] and [5.14], [DAH 16]).

Figure 1.24 (TF_i with i%) shows the optical constants of a layer of tholins on Al–SiO_2 determined with the Tauc–Lorentz model for various percentages of methane in the initial gas mixtures of 1%, 2%, 5% and 10%. The initial quantity of CH_4 injected into the reactor is about twice that involved in the production of thin films.

The values are comparable to those obtained with the B-spline model ([MAH 12a, MAH 12b]). A strong dependency of optical constants correlated with the initial concentrations of methane in the gas phase of the mixture used for the fabrication of tholins is observed. The imaginary optical index (k) decreases with the initial concentration of CH_4 from 2.3×10^{-2} down to 2.7×10^{-3} at a wavelength of 1,000 nm, while the real optical index (n) increases from 1.48 to 1.58 at 1,000 nm.

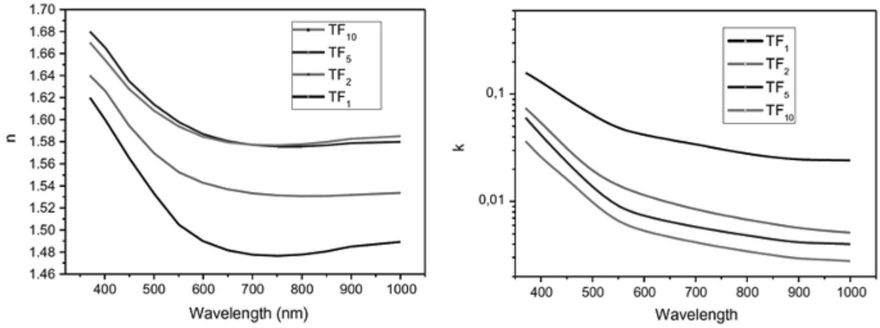

Figure 1.24. *Optical constants n and k of tholins between 400 nm and 1,000 nm for various initial concentrations (TFi: i%) of methane [MAH 12a]. For a color version of this figure, see www.iste.co.uk/dahoo/infrared2.zip*

The mid-IR spectra [SCI 10, CAR 12, MAH 12a, MAH 12b, GAU 12] recorded for thin films of tholins produced at various initial concentrations of methane are shown in Figure 1.25. Analysis of this spectrum shows that the increase in the signature of secondary and primary amines in absorption in mid-IR is correlated with higher absorption of tholins in the visible region (high k) for the thin layers produced when the percentage of methane is low. The signatures in mid-IR of VIMS (Visual and Infrared Mapping Spectrometer) and CIRS (Composite Infrared Spectrometer) are in agreement with an aerosol dominated by aliphatic carbon content.

The values of k of tholin films are compared to those of Titan aerosols deduced from Voyager [RAG 80] and Cassini/VIMS (Visual and Infrared Mapping Spectrometer) [RAN 10] observations (Figure 1.26).

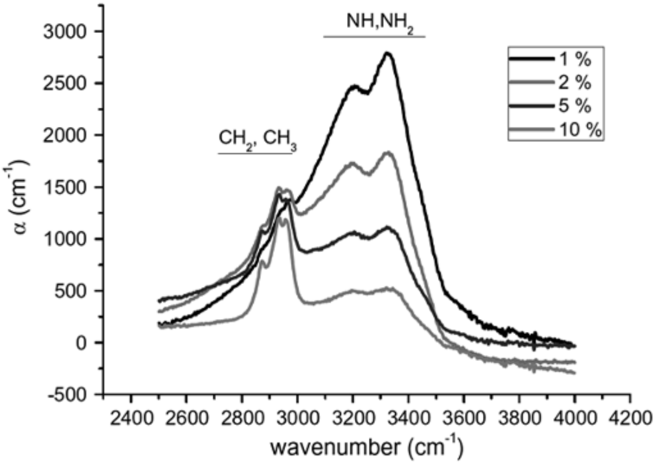

Figure 1.25. *Absorption spectra of tholins in mid-infrared for various initial concentrations of CH_4 [MAH 12a]. For a color version of this figure, see www.iste.co.uk/dahoo/infrared2.zip*

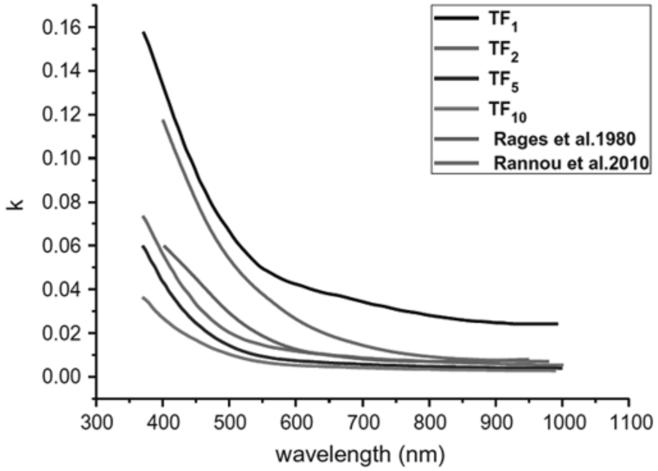

Figure 1.26. *Comparison of optical constants k of tholins for various initial concentrations (TFi: i%) of methane [MAH 12a] and the values deduced from data provided by planetary missions [RAG 80, RAN 10]. For a color version of this figure, see www.iste.co.uk/dahoo/infrared2.zip*

Rannou *et al.* [RAN 10] deduced their values from data provided by the DISR (Descent Imager/Spectral Radiometer) at low altitude (<140 m), using a model of scattering by fractal aggregates. The values of *k* thus obtained are particularly high and range between those of TF_1 (1%) and TF_2 (2%). These high values of *k* obtained from Titan observations are in definite disagreement with the aliphatic-rich aerosols. On the other hand, the extinction coefficient *k* calculated for Titan from Voyager data [RAG 80] is closer to the imaginary indices obtained for TF_2 (2%), TF_5 (5%) and TF_{10} (10%) which are relatively close to one another. A possible explanation for this apparent disagreement is the difference in the chemical composition of Titan aerosols at low and high altitudes. These conclusions on various compositions in the atmospheric layers of Titan seem to be supported by the works of Doose *et al.* [DOS 16] who reexamined the DISR (Descent Imager/Spectral Radiometer) data in the atmosphere of Titan with two constraints issued from measurements conducted outside the atmosphere, relying on the detection of layers of stratospheric clouds by the Cassini composite infrared spectrometer (CIRS). DISR data led to proposing three thin layers and a thicker layer of atmospheric aerosols. The initial aerosol model does not correspond to the geometric albedo or to the size of Titan's disc. The new aerosol model proposed by Doose *et al.* is compatible with DISR observations conducted inside and outside the atmosphere. DISR data correspond to a nearly constant low aerosol extinction coefficient at nearly 55 km altitude. The aerosols grow significantly darker from 200 km to approximately 80 km in altitude.

1.4.2. *Space-borne spectroscopy*

Mars Express (MEX) is the first European planetary mission on the Red Planet. The Mars Express orbiter (1,220 kg) was launched in June 2003 and placed on an elliptical polar orbit around Mars on December 25, 2003, with a pericenter altitude of 259 km, an apocenter altitude of 11,559 km and a period of 7.57 h. The spectroscopic study of the UV and IR signatures, characteristic of Mars' atmosphere, was conducted with a device referred to as the SPICAM (Spectroscopy for the Investigation of Characteristics of the Atmosphere of Mars). It is a spectrometer operating on an ultraviolet channel and a channel for IR radiation mainly dedicated to the study of Mars' atmosphere. It was developed through a collaboration between LATMOS (formerly Aeronomy Service: J.L. Bertaux) in France, BIRA-IASB (Royal Belgian Institute for Space Aeronomy: P. Simon) in Belgium and IKI (Russian Institute for Space Research: O. Korablev).

SPICAM is a light (4.7 kg) UV–IR double spectrometer, the first instrument to make stellar occultations on Mars. The UV imaging spectrometer (118–320 nm, resolution ≅ 1.5 nm, intensified CCD detector) was designed to obtain atmospheric vertical profiles and its fabrication relied on SPICAM plans, which was aboard Mars 96, which could not complete its mission. It is composed of two sets of instruments:

one for solar occultations, and one for stellar occultations and NADIR observation. SPICAM instrumentation is composed of two blocks: one sensor unit with a total mass of 3.8 kg, which comprises the UV and near-IR spectrometers, and a data processing unit (DPU, 0.9 kg) providing the interface of these two channels (Figure 1.27) with the spacecraft.

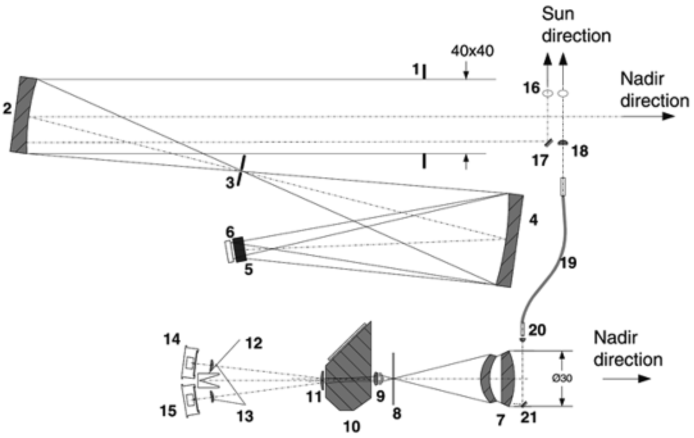

Figure 1.27. *Optical diagram of UV and IR channels of SPICAM light. (1) UV channel aperture; (2) off-axis parabolic mirror; (3) slit (mechanically - controlled aperture of variable width from wide to narrow); (4) concave UV grating; (5) intensifier; (6) CCD; (7) IR channel objective; (8) IR FOV diaphragm; (9) and (11) collimation lenses; (10) AOTF crystal; (12) light trap for non-diffracted light; (13) detector proximity lenses; (14) extraordinary beam detector; (15) ordinary beam detector; (16) solar aperture (closed by a shutter when the Sun is not observed); (17) and (21) plane mirror; (18) IR solar entry; (19) optical fiber; (20) fiber collimator [BER 06]. For a color version of this figure, see www.iste.co.uk/dahoo/infrared2.zip*

The UV imaging spectrometer (118–320 nm, resolution 1 nm, intensified CCD) of SPICAM is mainly dedicated to stellar occultations on Mars [BER 06]. The IR channel of SPICAM is a separate AOTF spectrometer integrated into the optical block of SPICAM with the UV spectrometer [NEV 06]. For the first time in planetary research, this spectrometer used acoustic-optic tunable filter (AOTF) technology, which allowed an unprecedented mass reduction for this type of instrument: 0.7 kg. The electrically controlled acoustic-optic filter sequentially scans the entire spectral range at a desired sampling rate, with random access. The absorption bands of H_2O (1.1 mm and 1.37 mm) are recorded with bands of CO_2 (1.43, 1.58 and 1.65 mm) making it possible to recover relative contents of H_2O. The near-IR albedo of Mars is measured with high spectral resolution, revealing bands characteristic of H_2O and CO_2 ice, though it is not possible to distinguish if the origin of these characteristics is related to the atmosphere (clouds) or to the surface (ice and frost). As expected, the emission of O_2 (a1D g) at 1.27 mm, occurring in the process of photodissociation of ozone, is easily detected by the IR SPICAM, allowing still another way to measure the ozone of Mars besides the UV measurements. The emission of O_2 (a1D g) allows the probing of altitudes mainly above 15–20 km; the reaction producing this emission is severely depleted by non-radiative quenching below this altitude. The two detectors of the AOTF spectrometer are sensitive to two orthogonal polarizations.

The ESA Venus Express orbiter was the first mission to apply solar and stellar occultation techniques to the atmosphere of Venus, with SPICAV/SOIR ((Solar Occultation in the Infra-Red) instruments. SPICAV (V for Venus) on the SPICAM model is composed of a series of three spectrometers with varied scientific objectives [BER 07].

SOIR is one of the three high-resolution spectrometers with a new optical design, which allows it to reach a resolution power of $\lambda / \Delta\lambda$ = 15,000–20,000 in a perfectly reasonable volume and mass (6 kg) balance, operating in the 2.2–4.3 μm range. It is the highest resolution achieved in planet exploration. The optical design comprises a high dispersion grating that operates at high orders and an acoustic-optic tunable filter (AOTF) to sort one order at a time. A detailed description of SOIR can be found in Nevejans *et al*. [NEV 06, VIL 08a], while in-flight performances are described in Mahieux *et al*. [MAH 08].

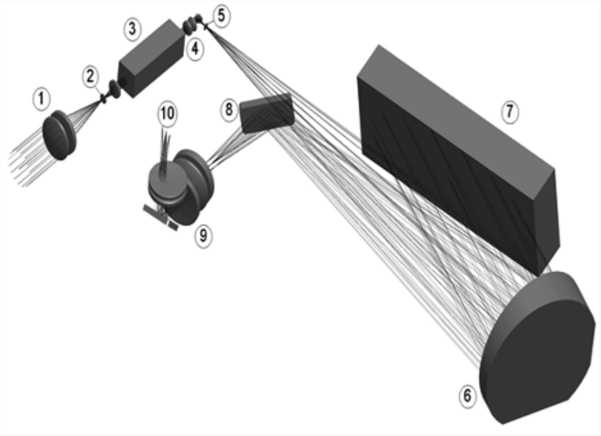

Figure 1.28. *Optical diagram of SOIR: (1) entrance optics, (2) diaphragm, (3) AOTF, (4) exit optics, (5) entrance slit of the spectrometer, (6) off-axis parabolic collimation and camera mirror, (7) echellette grating, (8) plane mirror, (9) detector optics and (10) detector assembly [NEV 06, MAH 08, VIL 08a]*

Venus is a very hot and dry planet, with a dense atmosphere mainly composed of carbon dioxide (CO_2, 96.5%) and nitrogen (N_2, 3.5%). Chemically active species, such as sulfur-based gases (OCS, SO_2) and halogenides (HCl, HF), had already been reported but since measurements had essentially already been conducted in the mesosphere below 100 km and below clouds, information on minor atmospheric components, their concentration, their reactions, their sources and their wells were incomplete. Venus is fully wrapped in clouds of enormous vertical extent of over 50 km. These clouds are mainly found in a permanent cloudy bridge located between 45 and 70 km altitude, with fine mists above and below. They are mainly composed of sulfuric acid (H_2SO_4) aerosol particles. SOIR is the only instrument aboard the Venus Express that can contribute to the study of this region. Above 100 km altitude, between 120 and 300 km, is the ionosphere composed mainly of O_+ and O_2^+ ions in the lower layers. Note the absence of a magnetic field on Venus.

The main objective assigned to SOIR was to determine the vertical distribution of HDO and H_2O, as high as possible in the atmosphere, to see whether a splitting mechanism (such as condensation) existed that would modify the D/H ratio in the upper atmosphere, and perhaps prevent D atoms from escaping Venus. In fact, as previously reported [BER 07], the HDO/H_2O ratio does not vary much with altitude until 90 km. Thanks to a high spectral resolution power of R ~ 15,000–20,000, unprecedented in space exploration using SOIR, a new gas absorption band was rapidly detected in the atmospheric transmission spectra around 2,982 cm^{-1}, showing a structure resembling a non-resolved Q-branch and a number of isolated lines with a regular profile. This absorption was not correlated to any species contained in the HITRAN or GEISA databases at that time but was found to be very similar to an absorption model observed by an American team in the spectrum of solar light reflected by the ground of Mars [VIL 08b]. In the scientific literature, an absorption around 2,982 cm^{-1} is typical for an asymmetric C–H bond, and research in other databases, mainly of organic materials, was conducted. None of the absorption characteristics found near 2,982 cm^{-1} correspond to the observed signature. Finally, this team suggested that the absorption was due to an uncatalogued transition of the molecule $^{16}O^{12}C^{18}O$. The possible existence of this isotopic species of CO_2 was quickly confirmed by theoretical considerations by Perevalov and Tachkun [BER 08].

The discovery and attribution of the observed transitions were thus described by Bertaux *et al.* [BER 08]. “Then on December 22, 2006 one of us (Bertaux) received a message from Mike Mumma, asking what SOIR was seeing on Venus around 2,982 cm^{-1}, and willing to compare to a new absorption feature that his group had detected in the solar spectrum scattered by Mars, as observed from the Earth’s ground. When we compared the signatures, they were identical (within error bars). It should have rang a bell in our mind: what is most common to Venus and Mars atmosphere? CO_2! In spite of this hint, we continued to search for organic material signature, until the group of Mumma and colleagues proposed to us in April 2007 that the absorption signature common to Mars and Venus was due to an uncatalogued band of 628 CO_2 isotope (628 standing by convention for $^{16}O^{12}C^{18}O$, dropping the 1 in front of 16, 12, 18). This identification was soon after confirmed by Perevalov and Tashkun (personal communication) on theoretical grounds."

It is the $v_2 + v_3$ vibration–rotation transition. Its existence in this region of the spectrum could have been predicted from the study of transitions of 628 CO_2 molecules observed, either in the gas phase or in argon and krypton matrices, giving the energy levels of v_2 (656.09 cm^{-1}) and v_3 (2,323.91 cm^{-1}) transitions (Dahoo *et al.* [DAH 06]), with $v_2 + v_3 = 2{,}980.0\ cm^{-1}$. This transition does not exist for the main isotopologue 626 of CO_2, as it is forbidden by the symmetry of the molecule, which being linear, has an inversion center. The replacement of one ^{16}O atom by a ^{18}O atom breaks the symmetry, making the transition possible for the 628 CO_2 variety. The selection rules also allow transitions with $\Delta l = 1$, where l is the quantum number of internal rotation for the degenerate mode v_2. A central line can then be observed at 2,982.0 cm^{-1} since 2,980.0 cm^{-1} corresponds to $\Delta l = 0$. It is important to note that for a symmetric molecule (626 or 636), besides $\Delta l = 1$, the transitions are not authorized unless at the same time $\Delta V_2 + \Delta V_3$ is odd, where V_2 and V_3 are vibrational quantum numbers of modes v_2 and v_3, respectively. Hence, SOIR led to the discovery of this absorption of the isotopic variety of CO_2 in the atmosphere of Venus, making it possible to exclude any confusion with an absorption by C–H bonds. This discovery highlights the role of CO_2 isotopologues (as well as that of H_2O and HDO) as important greenhouse gases in the atmosphere of Venus.

1.4.3. *LIDAR spectroscopy for space observation*

The measurement of the profile of the atmospheric concentrations of particles (aerosols), water vapor and ozone depending on the altitude H, requires either measurements from planes or balloons, or techniques that rely on the use of a high power pulsed LASER (Figure 1.29). The first LIDAR (LIght Detection And Ranging) measurements were conducted in 1968 in Sierra Nevada and the first publications were authored by Collis *et al.* [COL 68, VIE 73]. According to the studies, pulsed lasers could be used for locating clouds and aerosols and studying the atmospheric dynamics. The LIDAR equipment, which consists of a laser scanner, a global positioning system (GPS) and an inertial navigation system (INS), can be airborne on a small plane. The laser sends short pulses to the ground surface, which reflects them or sends them back to the laser emission device. Detecting the return pulses, the equipment records the time needed for the pulse to travel from the laser scanner to the ground and back. The distance between the laser and the ground is then calculated according to the speed of light.

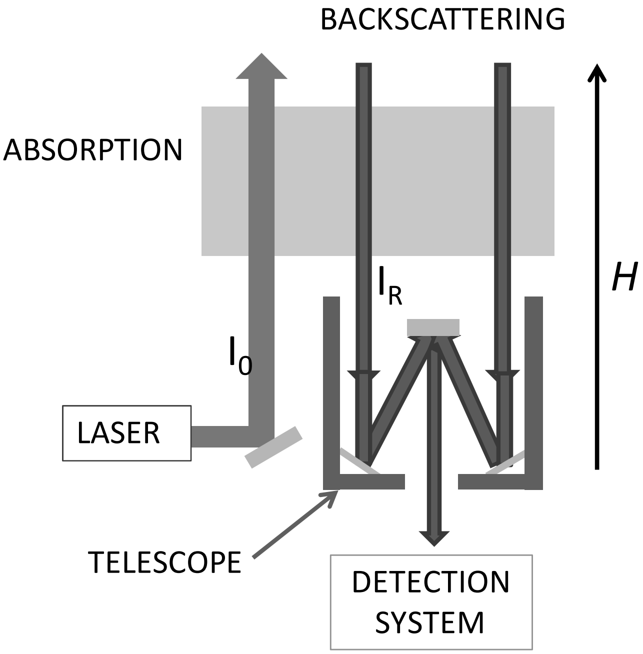

Figure 1.29. *Diagram of the LIDAR operating principle. For a color version of this figure, see www.iste.co.uk/dahoo/infrared2.zip*

The operating principle of a LIDAR relies on the backscattering of an electromagnetic wave in the visible range, similar to RADARs, which operate in the microwave range. A short and intense laser pulse is sent vertically into the atmosphere. The molecules and particles of the atmosphere absorb, transmit and scatter the laser light. A small part of the energy emitted by the laser is backscattered by aerosols in the atmosphere in the direction of a telescope and of a detection chain measuring the backscattered intensity IR(t) as a function of time. The backscattered wave detected by the LIDAR carries information on the properties of the atmosphere. The wave collected by the LIDAR system after propagation through the atmosphere and backscattering by an aerosol is obviously of very low intensity and its detection is not easy. A direct detection system or heterodyne detection can be used. The analysis of parameters such as intensity, backscattered wave frequency delay or offset leads to data that carries some amount of information and knowledge. Intensity measurement provides quantitative information on aerosol concentration. The delay gives the distance traveled by the laser and therefore the position of aerosols. The frequency offset gives the speed by Doppler effect.

The LIDAR equation is expressed as:

$$n(l) = n^0 \Gamma(l) \frac{S}{l^2} \beta(l) \frac{c\tau_D}{2} \exp\left[-2\int_0^l \alpha(z)dz \right] \quad [1.47]$$

where $\alpha(z)$ is the extinction coefficient of air at altitude z, β is the backscattering coefficient of the air volume in the layer thickness, n is the number of detected photons depending on the number of particles in this layer, and n^0 is the number of initial photons in the initial pulse. The solid angle under which the backscattered photons are detected is assumed to be equal to S/l^2 and the detection efficiency is given by the parameter $\Gamma(l)$ (Figure 1.30).

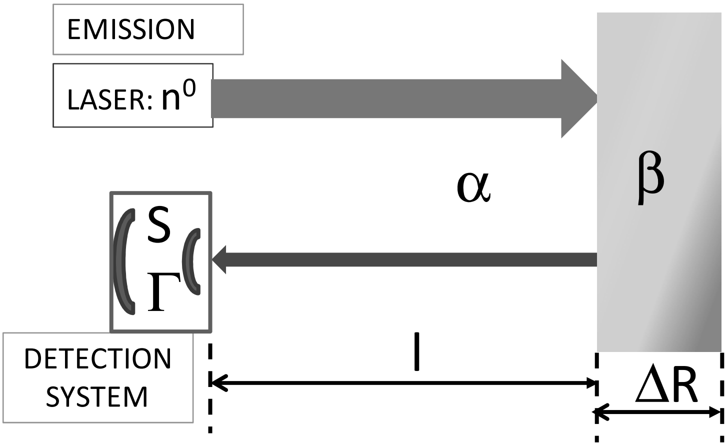

Figure 1.30. *Diagram of LIDAR measurement parameters. For a color version of this figure, see www.iste.co.uk/dahoo/infrared2.zip*

The number of backscattered photons is proportional to the number of initial photons n^0 in the initial pulse; $\Gamma(l)$, the detection efficiency depends on path l, as the number of backscattered photons depends on l and Γ depends on the number of photons collected by the detector. The number of collected photons is limited by the solid angle S/l^2 of the telescope aperture. β, the backscattering coefficient of the air volume in the layer thickness, also depends on path l. In the integral, factor 2 corresponds to the return path and the integral corresponds to the continuous sum of various factors involved in the extinction of light (absorptions, scattering, reflection coefficient, etc.) depending on the dimensions and properties of the particles encountered on the laser path.

The backscattering and extinction coefficients can be calculated from the interaction between light and the air components. If the laser wavelength is within the absorption band of a species, the extinction coefficient splits into two parts: $\alpha_{tot}(z) = \alpha(z) + \sigma C(z)$, where σ is the absorption cross section for the species, and C(z) its concentration at altitude *z*. In this case, in order to take into account the species absorption, the LIDAR equation is written as:

$$n(l) = n^0 \Gamma(l) \, {}^{S}\!/_{l^2} \, \beta(l) \, {}^{c\tau_D}\!/_{2} \exp(-2 \int_0^l (\alpha(z) + \sigma C(z))) dz \qquad [1.48]$$

In terms of emitted power P^0 and detected power *P*, the detector response τ_D can be replaced by the laser pulse duration τ, *n(l)* and n^0 can be replaced, respectively, by *P(l)* and P^0 to obtain:

$$P(l) = P^0 \Gamma(l) \, {}^{S}\!/_{l^2} \, \beta(l) \, {}^{c\tau}\!/_{2} \exp(-2 \int_0^l (\alpha(z) + \sigma C(z))) dz \qquad [1.49]$$

The detection chain measures an intensity $I_R(t)$ that depends on time. Assuming that the laser emits a pulse between the very close instants $t = 0$ and $t = \tau$, there is a simple relation between the distance 1 of particles that backscatter light and the instant of the pulse return. Indeed, the scattering corresponding to the start of the pulse emitted at t=0 returns at instant $t_1 = 2l/c$ and that corresponding to the end emitted at τ returns at instant $t_2 = \tau + 2l/c$, where *2l* corresponds to the back and forth path. The maximum duration of the laser pulse so that the spatial resolution of the LIDAR Δl in altitude is of about 20 m, for example, is in this case given by $2\Delta l/c$; thus, 133 ns. If τ_D is the response time of photons backscattered by the detector towards the active surface of the telescope S, then the thickness ΔR of the observable layer is given by $\Delta R = 2c\tau_D$

Elastic scattering (without frequency change) depends on the size of the particles: Mie scattering ($\lambda << d$) and Rayleigh scattering ($d << \lambda$). Consequently, Rayleigh scattering is due to molecules, while Mie scattering is due to aerosols, since the maximum size of molecules is of the order of nm and that of aerosols is of the order of µm.

A particularly important application of LIDARs is the Doppler wind LIDAR, used in meteorology, which uses the backscattering of erbium laser light (wavelength of 1.56 µm, harmless to the eyes) on the aerosols in the atmosphere (Figure 1.31).

For example, LIDAR measurements contribute to the reliability of meteorological predictions. A spatial resolution of the order of the meter corresponds to a temporal resolution Δt of the detection system of about 6 ns, which is feasible. The minimal bandwidth Δf of detection electronics is in this case equal to 30 MHz and is determined by Fourier transform.

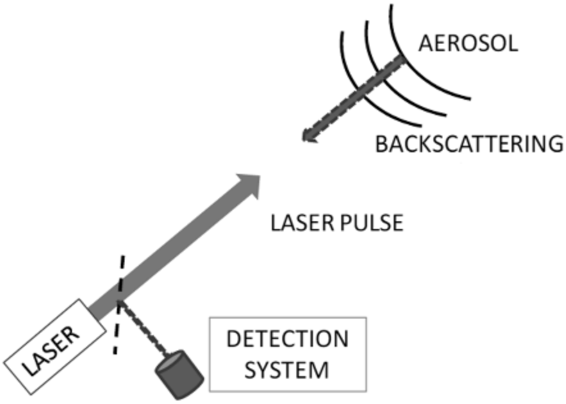

Figure 1.31. *Diagram of the Doppler wind LIDAR observation principle. For a color version of this figure, see www.iste.co.uk/dahoo/infrared2.zip*

1.5. Conclusion

This chapter presented several measuring instruments that are used in the laboratory to observe the IR spectra of molecules. These techniques are based on wave interference by Fourier transform or the various measurement methods based on laser spectroscopy aimed at achieving better precision in absorption measurements, at being able to measure weak transitions or finally at identifying species present in negligible quantities. An example of a technique using polarized light through spectroscopic ellipsometry was also provided for the characterization of aerosols in the solid phase, such as the tholins present in the atmosphere of Titan orbiting Saturn. This chapter also presented an example of observation instruments aboard orbiters (Mars Express and Venus Express) allowing better identification of the nature of the observed species (628 CO_2 variety or other isotopic species). Other instruments such as the LIDAR are used for the study of molecules and complete the panorama of different devices, which are part of a larger set of instruments used for the spectroscopic study of molecules.

1.6. Appendices

1.6.1. *Appendix 1: Measurement distortion and data processing*

The observation or detection of an absorption line requires further processing to determine its intensity. It is the result of measurement distortion inherent in any measurement by an instrument and which requires the processing of collected data.

In general, the recorded spectrum $A_O(\sigma)$ of a line is the convolution product of the apparatus function $f(\sigma)$ and of the real shape $A_v(\sigma)$ of the line. Parameters such as intensity, width and center of an absorption line are obtained after line deconvolution. The relation between $A_O(\sigma)$ and $A_v(\sigma)$ is expressed as an integral:

$$A_O(\sigma_0) = \int_{\sigma_{min}}^{\sigma_{max}} f(\sigma - \sigma_0) A_V(\sigma) d\sigma$$

where the integral is calculated over the spectral range of the absorption line.

In general, the method used for line deconvolution relies on the criteria of the sampling theorem, which is applied to determine the adequate sampling interval for digitizing the continuous spectrum. The deconvolution of the recorded spectrum is then conducted digitally by algorithms based on the sampling theorem.

Consider $h(x) = f(x)*g(x)$, the convolution product of two real functions. $F(\nu) = TF\ f(x)$ and $G(\nu) = TF\ g(x)$ are the Fourier transforms of $f(x)$ and of $g(x)$ of finite domain $[-1/2h_0, +1/2h_0]$. Using the sampling theorem with an interval h_0, this product can be written as an infinite series. Applying the sampling theorem to the function $f(x)$ leads to expressing $f(x)$ in the following form:

$$f(x) = P_h\, f(x) * sinc\ ({}^{x}/_{h})$$

where sinc $(x/h) = sin(\pi x)/\pi x$ and $P_h f(x)$ is the sampled function of $f(x)$ of interval h such that:

$$P_h\, f(x) = \sum_{-\infty}^{+\infty} f(ph) \,.\, \delta(x - ph)$$

where $f(ph)$ are the values of function $f(x)$ at points ph.

Considering the above equations, the convolution product $h(x)$ is expressed in the following form:

$$h(x) = \sum_{-\infty}^{+\infty} f(ph) \,.\, \delta(x - ph) * sinc\ ({}^{x}/_{h}) * g(x)$$

In the Fourier space, the expression of this equation is given by:

$$H(\nu) = TF \left(\sum_{-\infty}^{+\infty} f(ph) \,.\, \delta(x - ph) \right) .\, h\, rect\ (h\nu) .\, G(\nu)$$

where $h\ rect\ (h\nu)$ is the Fourier transform of sinc x/h, such that:

$$rect\ (h\nu) \begin{cases} = 1 & |\nu| < {}^{1}/_{2h} \\ = 0 & |\nu| > {}^{1}/_{2h} \end{cases}$$

Since $h < h_0$, $[-1/2h_0, +1/2h_0]$, the domain of $G(\nu)$ is smaller than that of $rect\ h\nu$, $[-1/2h, +1/2h]$, the multiplication by $rect\ h$ amounts to multiplying by 1, so that $H(\nu)$is finally written as:

$$H(\nu) = TF\left(\sum_{-\infty}^{+\infty} f(ph)\,.\,\delta(x - ph)\right).\,h.\,G(\nu)$$

After inverse Fourier transform, this expression yields:

$$h(x) = \sum_{-\infty}^{+\infty} f(ph)\,.\,\delta(x - ph) * hg(x)$$

Since the convolution of the Dirac distribution $\delta(x - ph)$ and $g(x)$ corresponds to a translation of the function $g(x)$ such that $\delta\ (x - ph) * g(x) = g\ (x - ph)$, the expression of $h(x)$ is given by:

$$h(x) = \sum_{-\infty}^{+\infty} hf(ph)\,.\,g(x - ph)$$

The numerical process relies on this result to build equivalent convolution products from an expansion limited to a maximum value N of the number of sampling points. $f(x)$ is rewritten as:

$$f(x) = \sum_{-\infty}^{+\infty} hf(ph)\,.\,\delta(x - ph) * {}^{1}/_{h}\, sinc\ ({}^{x}/_{h})$$

which leads to:

$$f(x) = \sum_{-\infty}^{+\infty} f(ph)\,.\,sinc\left({}^{(x - ph)}/_{h}\right), \quad h < h_0$$

Limiting this expansion to a finite number N of terms, the following function is calculated:

$$f^N(x) = \sum_{-N}^{+N} f(ph).sinc\left({(x - ph)}/{h}\right), \quad h < h_0$$

which is a quadratic mean approximation over $]-\infty, +\infty[$, using an adequate expansion basis such that:

$$\int_{-\infty}^{+\infty} |f(x) - f^N(x)|^2 \, dx = min$$

The following convolution product is then calculated:

$$h(x) = \sum_{-\infty}^{+\infty} hf^N(ph).g(x - ph)$$

of the function $f^N(x)$ and the function $g(x)$ whose spectrum does not contain the frequencies that are higher than those of $F(\nu)$. The best approximation is obtained for $h = h_0$.

In practice, if $A_{exp}(\sigma) = E_a(i)/E_0(i)$ denotes the recorded spectrum, where $E_a(i)$ is the value of the signal detected as a function of the wave number σ and $E_0(i)$ is the signal detected in the absence of absorbing gas, this spectrum is compared to a calculated spectrum $A_{th}(\sigma) = A(\sigma) * f(\sigma)$. For example, $A(\sigma) = 1- exp(-k(\sigma,p)l)$, for an isolated line where P is the gas pressure, l is the length traveled in the gas and k is the profile of the line that can be that of a Doppler broadened line, or of a pressure broadened line (Chapter 3, Volume 1, [DAH 17]).

A minimization process is applied to:

$$\int_{-\infty}^{+\infty} \left|A_{exp}(\sigma) - A_{th}(\sigma)\right|^2 d\sigma = min$$

The nonlinear simplex method, also referred to as the Nelder–Mead method [NEL 65, PRE 86, pp. 521–528], is often used as it is a zeroth-order method that does not require a gradient calculation. Other algorithms based on the calculation of the gradient of the function to be minimized for the evaluation of second-order derivatives are nevertheless also used, such as the LM [LEV 44, MAR 63] or Broyden–Fletcher–Goldfarb–Shanno (BFGS) [BRO 69, FLE 70, GOL 70, SHA 70] algorithms.

The minimization process is conducted as follows. Consider an N-dimensional space whose points M have the values $(x_1, x_2, ...x_N)$ as coordinates. Each point M in space is associated with the value $f(x_1, x_2, ...x_N)$ of the function to minimize. Starting from an arbitrary point M_1, of value $f(M_1)$, the coordinates of M_1 are increased by $(\Delta x_1, \Delta x_2, ...\Delta x_N)$. $N + 1$ points are defined, as well as the values associated by f of N new coordinates:

Coordinates of M_1: $x_1, x_2, ...x_N$ and $f(M_1)$

Coordinates of M_2: $x_1+\Delta x_1, x_2, ...x_N$ and $f(M_2)$

Coordinates of M_3: $x_1, x_2+\Delta x_2, ...x_N$ and $f(M_3)$

…

Coordinates of M_{N+1}: $x_1, x_2, ...x_N +\Delta x_N$ and $f(M_{N+1})$

Proceeding from these points, which are classified in ascending order of the value of $f(M_i)$, the worst point, the one that has the maximum value, is replaced by a better point, and so on, using the procedure of the chosen method. In the end, the expected profile is reached such that the intensity of the line can be calculated, for example.

The nonlinear optimization algorithm of Nelder and Mead [NEL 65] relies on Dantzig's simplex model [DAN 90], a geometric method that uses N parameters to build a simplex of $N + 1$ vertices to which a certain number of operations is applied. If the function to minimize has two variables, the simplex is a triangle, if it has three variables, the simplex is a tetrahedron. An algorithm that involves the comparison of the values of the function $f(x_1, x_2, ...x_N)$ to be determined is applied to each vertex of the simplex. The vertex that yields the worst value (the highest) is replaced by a new vertex. The values of $f(x'_1, x'_2, ...x'_N)$ are recalculated, and the search for the minimum continues. This process generates a sequence of simplexes for which the values of the function at vertices are increasingly small. In principle, the hypersurface of simplexes gradually diminishes and the coordinates of the minimum are thus obtained.

This criterion is not necessarily achieved at each stage where a point is replaced by a better one. In this case, the simplex is subjected to other operations: reflection (volume preservation), expansion (volume increase) or contraction or multidimensional contraction (volume decrease near solution). At each transformation, the criterion function is evaluated to find a better point than the one calculated in the previous stage. The process is continued until the stage corresponding to the stop criterion (value below or equal to the fixed threshold).

If the number of variables is n, a general simplex with $n+1$ vertices is built from n initial values by successively applying an increase to each starting value. These operations can be implemented on the simplex, for example, by sorting the vertices of the simplex following the value of the cost function in order to select three vertices having, respectively, the best score, the worst score and the second last. The vertex with the worst score is replaced by symmetry of the simplex with respect to the hyperplane defined by the other vertices, which amounts to conducting a research in a direction opposite to the one that yielded the bad score. If the cost function is improved, then an expansion occurs; otherwise, a one-dimensional contraction takes place. If despite this, the cost function does not improve, the algorithm makes a multidimensional contraction in several directions. The vertex associated with the maximum value of $f(x_1, x_2, ...x_N)$ is replaced by a point in the space of n variables, which leads to a lower corresponding value of $f(x'_1, x'_2, ...x'_N)$.

Considering the example of a function with two variables $f(x, y)$, the simplex is a triangle. $S_1(x_1, y_1)$, $S_2(x_2,y_2)$ and $S_3(x_3,y_3)$ denote the vertices of the simplex and $z_k = f(S_k)$, the values calculated at vertices S_k, $k = 1, 2, 3$. The values calculated at vertices S_k, $k = 1, 2, 3$ in ascending order are denoted by m (minimum), μ (mean) and M (maximum). The vertex corresponding to M must be replaced. The algorithm of the simplex is achieved by calculating:

1) the mid-point:

$$S_M = (f^{-1}(m) + f^{-1}(\mu))/2;$$

2) the vertex reached by reflection:

$$S_R = S_M + (S_M - f^{-1}(M)) = 2S_M - f^{-1}(M);$$

3) the vertex reached by expansion:

$$S_D = S_R + (S_R - S_M) = 2\, S_R - S_M;$$

4) the vertex reached by contraction: S_C from the two possible vertices for contraction: $C_1 = (f^{-1}(M) + S_M)/2$ and $C_2 = (S_M + S_R)/2$ and of the condition: if $f(C_1) < f(C_2)$, then $S_C = C_1$, else $S_C = C_2$;

5) the best vertex:

$$S_F = (f^{-1}(M) + f^{-1}(m))/2.$$

The following algorithm is then applied, if $f(S_R) < \mu$, then apply case I, else case II:

– case I: if ($m < f(S_R)$), then replace $f^{-1}(M)$ by S_R, else calculate S_D and if ($f(S_D) < \mu$), replace $f^{-1}(M)$ by S_D, else replace $f^{-1}(M)$ by S_R;

– case II: if ($f(S_R) < M$), then replace $f^{-1}(M)$ by S_R. If $f(S_R) \geq M$, then calculate S_C and if $f(S_C) < M$, then replace $f^{-1}(M)$ by S_C, else calculate S_F replace $f^{-1}(M)$ by S_F and replace $f^{-1}(\mu)$ by S_M.